Silicon isotopes reveal the impact of fjordic processes on the transport of reactive silicon from glaciers to coastal regions

Tong Wang [a,*], Hong Chin Ng [a,b], Jade E. Hatton [c], Samantha J. Hammond [d],
E. Malcolm S. Woodward [e], Lorenz Meire [f,g], Katharine R. Hendry [a,h]

[a] School of Earth Sciences, University of Bristol, Bristol, UK
[b] Laboratoire Géosciences Océan, Ifremer - UBO - CNRS, Plouzané, France
[c] Department of Ecology, Charles University, Prague, Czech Republic
[d] School of Environment, Earth, and Ecosystem Sciences, The Open University, Milton Keynes, UK
[e] Plymouth Marine Laboratory, Prospect Place, The Hoe, Plymouth, UK
[f] Greenland Climate Research Centre, Greenland Institute of Natural Resources, Nuuk, Greenland
[g] Department of Estuarine and Delta Systems, Royal Netherlands Institute for Sea Research, Yerseke, the Netherlands
[h] Polar Oceans Team, British Antarctic Survey, Cambridge, UK

ARTICLE INFO

ABSTRACT

Accelerated mass loss from the Greenland Ice Sheet leads to retreating glaciers and enhanced freshwater runoff to adjacent coastal regions, potentially providing additional essential nutrients, such as silicon, to downstream primary producers. However, the role of fjordic sediments in modulating the supply of silicon from glacial environments to marine ecosystems remains poorly constrained, particularly for the quantification of silicon fluxes from the sediments into overlying waters in high-latitude fjordic systems. In this study, we use the concentration and stable isotopic composition of dissolved silicon in pore waters and core-top waters, and amorphous silica phases (such as glacially-derived amorphous silica) in sediments and suspended particulate matter, collected from two fjords in the southwest Greenland margin to address this knowledge gap. We combine downcore observations with core incubations and isotope mass balance approaches to assess the benthic flux of dissolved silicon and deconvolve potential contributors to this flux during early diagenesis. Our results suggest that molecular diffusion only accounts for a portion of benthic dissolved silicon transport. Relative to surrounding continental shelves and highly-productive open ocean waters, the estimated benthic dissolved silicon flux at our sites is smaller in magnitude, supporting the role of fjords as a 'trap' for reactive silicon in high-latitude systems.

1. Introduction

Fjords, formed by glacial activity, are critical zones for glacier-ocean interactions, and are locations where heat, salt, nutrients, and other elements are exchanged between meteoric waters and marine-sourced waters from adjacent coastal regions (Hopwood et al., 2020; Sen et al., 2022). They are also active bioreactors acting as sinks, conduits, and filters for carbon (C) and other nutrients (Bianchi et al., 2020). Recent studies have identified that subglacial silicate weathering generates dissolved silicon (DSi) and secondary weathering products, such as soluble amorphous silica (ASi), which are attached to glacially-sourced fine-grained suspended particulate matter (SPM) (Frings et al., 2016; Hatton et al., 2019; Hatton et al., 2023). Thus, glacial runoff, including surface meltwater runoff, subglacial freshwater discharge and iceberg-entrained debris, exports an additional high DSi + ASi flux, making glaciers and ice sheets significant dynamic components of polar silicon (Si) cycling (Meire et al., 2016; Hawkings et al., 2017; Hatton et al., 2019). However, there is still a lack of research focused on the biogeochemical cycling of the glacially-derived abiogenic ASi described above in high-latitude fjords and fjordic sediments, despite the potentially critical implications for the availability of this nutrient to primary producers.

Spring blooms in fjords are typically dominated by diatoms, a group of photosynthesizing microalgae that have an absolute requirement for silicic acid (H_4SiO_4), the main form of DSi in seawater, to precipitate biogenic silica (BSi) as a protective shell or frustule (Krause et al., 2018;

Krause et al., 2019). Due to the undersaturation of seawater with respect to DSi, the BSi remains of dead diatoms and more reactive abiogenic ASi phases (e.g., glacially-derived ASi) will dissolve as they sink through the water column (Frings, 2017; Ward et al., 2022a). Any BSi and glacial ASi deposited on the seafloor will likely continue to dissolve during burial processes (Tréguer et al., 2021). Remineralization enriches pore waters in dissolved nutrients relative to overlying bottom waters (Rutgers Van Der Loeff, 1980), and results in a concentration gradient that drives nutrient flow from sediment to water through molecular diffusion, bioturbation, bioirrigation, and other processes within sediments that drive pore water advection and mixing (Huettel et al., 1998; Janssen et al., 2005; Schulz and Zabel, 2006; Aller, 2014). Recycled DSi can potentially be supplied back to the euphotic zone as a bioavailable nutrient, and thus can be reused for new diatom growth via upwelling and mixing, hence closing the pelagic-benthic loop (Tréguer and De La Rocha, 2013; März et al., 2015; Hou et al., 2019).

In marine sediments, the preservation and recycling of reactive particulate silicon (BSi, ASi) are controlled by the balance between dissolution and precipitation processes (Geilert et al., 2020a). Given the undersaturated pore water environments, the dissolution of soluble amorphous silica mainly controls the accumulation of pore water DSi (Aller, 2014; Geilert et al., 2020a), with additional contribution from the dissolution of other biogenic phases such as siliceous sponge spicules (Ng et al., 2020), and radiolarian tests (Maldonado et al., 2019), dissolution of lithogenic (non-biological) minerals (Geilert et al., 2020a; Ward et al., 2022a), and desorption from amorphous iron (Fe)-Si minerals (Ng et al., 2022). The dissolution kinetics of ASi is also moderated by the incorporation of terrigenous-released aluminium (Al) and Fe into the surface structure (Aller, 2014; Geilert et al., 2020a) and the precipitation of authigenic aluminosilicates (Michalopoulos and Aller, 2004; Ehlert et al., 2016). This latter process, termed reverse weathering, involves the precipitation of cation-rich aluminosilicates from reactive Si phases (e.g., BSi, or poorly crystalline secondary weathering products) within the sediments during early diagenesis, impacting the alkalinity produced during silicate weathering and the mass balance of several key metals in the oceans (Mackenzie and Garrels, 1966; Michalopoulos and Aller, 1995; Aller, 2014; Baronas et al., 2016; Frings et al., 2016; Sutton et al., 2018a; Rahman, 2019; Krissansen-Totton and Catling, 2020). Furthermore, the authigenic precipitation of aluminosilicates in marine sediments likely plays an important role in increasing the preservation potential for reactive Si phases (i.e., ASi), significantly impacting the global Si biogeochemical cycle (Aller, 2014; Frings et al., 2016; Ward et al., 2022a).

Redox conditions can also influence pore water DSi build-up through sediment Fe cycling. Pore water Fe availability is mainly controlled by redox states, where dissolved Fe^{2+} is released via Fe(III)-rich mineral reduction and reprecipitated into Fe oxy-hydroxides in oxidated sediments, or pyrite in anoxic, sulphide-rich sediments (Aller, 2014; Ng et al., 2022). Pore water DSi can adsorb onto Fe oxy-hydroxides and co-precipitate forming amorphous Fe—Si minerals (Delstanche et al., 2009; Zheng et al., 2016; Geilert et al., 2020a; Schulz et al., 2022). The balance between competing DSi release and uptake processes during early diagenesis acts to impact DSi fluxes and Si storage in seabed sediments (Sutton et al., 2018a).

There are three naturally occurring stable isotopes of Si: ^{28}Si, ^{29}Si, and ^{30}Si, with abundances of 92.2 %, 4.7 %, and 3.1 %, respectively (de Laeter et al., 2003). Different Si pools are characterized by different Si isotopic compositions (denoted by $\delta^{30}Si$), which are driven by a combination of the Si source and any isotopic fractionation associated with subsequent reactions or transformations within or between pools (Sutton et al., 2018a). In marine sediments, $\delta^{30}Si$ is a powerful tracer for different early diagenetic reactions due to their different isotopic fractionation behaviours (Tatzel et al., 2015; Geilert et al., 2016; Cassarino et al., 2020). For example, the dissolution of glacial ASi, with $\delta^{30}Si$ values (denoted by $\delta^{30}Si_{ASi}$) varying from −0.47 ‰ to −0.22 ‰ (Hawkings et al., 2018b; Hatton et al., 2019), usually introduces a more

negative $\delta^{30}Si$ signal into pore waters in fjordic sediments, when assuming that there is no fractionation during ASi dissolution (Wetzel et al., 2014). The lighter ^{28}Si isotope is preferentially adsorbed onto Fe oxy-hydroxides and incorporated into secondary authigenic minerals and amorphous precipitates through early diagenetic processes, leaving the remaining substrate enriched in the heavier isotopes (Delstanche et al., 2009; Ehlert et al., 2016; Geilert et al., 2016; Zheng et al., 2016; Pickering et al., 2020; Closset et al., 2022; Ng et al., 2022). The Si isotope fractionation factor associated with the precipitation of authigenic clays has been estimated to vary from −1.8 ‰ to −2.2 ‰ in riverine and terrestrial settings (Ziegler et al., 2005a; Ziegler et al., 2005b; Opfergelt and Delmelle, 2012; Hughes et al., 2013), and up to −3 ‰ in deep-sea environments (Geilert et al., 2020b).

Pore water DSi accumulation is controlled by the dissolution of ASi and terrigenous minerals, the reprecipitation of authigenic aluminosilicates, and reactions associated with Fe oxy-hydroxides (März et al., 2015; Geilert et al., 2020a; Ng et al., 2020; Ng et al., 2022). Any isotopic fractionation during these processes, therefore, could result in shifts in the $\delta^{30}Si$ value of DSi within the pore fluids (Ehlert et al., 2016). As such, the stable isotopic composition of sediments and in particular pore waters can be used to trace benthic Si cycling, and as a means to deconvolve the different contributors of net DSi efflux from the sediments during early diagenesis (Ehlert et al., 2016; Cassarino et al., 2020; Geilert et al., 2020a; Ng et al., 2020; Closset et al., 2022; Ng et al., 2022; Ward et al., 2022a).

There has only been one study that has evaluated benthic DSi fluxes in a fjordic setting, which was at the Chilean Patagonian fjords (Ng et al., 2022). The authors there suggest that benthic DSi fluxes near fjord heads are significantly smaller than those in the coastal ocean, but this interpretation has been based on a global compilation of coastal ocean benthic DSi flux, not a direct comparison with a proximal coastal site off Chilean Patagonia.

This current study focuses on examining the understudied benthic Si cycling under the setting of an enhanced input of reactive glacier-sourced ASi phases at and close to fjord heads. The study aims to evaluate benthic DSi fluxes in fjords situated in Greenland, in the northern hemisphere and to identify and discuss processes that influence the magnitude of the evaluated benthic flux, and to directly compare the benthic DSi fluxes of two Greenland fjords (one connected to land-terminating glaciers and the other connected to both land-terminating and marine terminating glaciers) with those in local coastal waters. We use two approaches to evaluate the flux of DSi from fjordic sediments to the overlying water column. Molecular diffusion flux of DSi is calculated from pore water DSi profiles, and the total DSi flux is estimated from a core incubation experiment.

2. Materials and methods

2.1. Study sites and field sampling

Hydrographic and biogeochemical data were collected in two fjords adjacent to the GrIS, Ameralik Fjord (AM) and Nuup Kangerlua (Godthåbsfjord, GF). Ameralik Fjord is located on the southwest margin of Greenland close to Nuuk (Fig. 1a), with a length of 75 km and covering an area of about 400 km² (Stuart-Lee et al., 2021). The fjord is land-terminating, i.e., glacial meltwater enters the fjord via a proglacial system, fed by the glacial river Naajat Kuuat (NK) (Fig. 1a).

Nuup Kangerlua is a large multi-branch sub-Arctic fjord close to Ameralik Fjord on the northern side (Fig. 1a) with a main fjord branch of 190 km and the whole fjord system covers a surface area of 2013 km² (Meire et al., 2017; Mortensen et al., 2018). Nuup Kangerlua is in contact with three marine-terminating glaciers: Kangiata Nunaata Sermia (KNS), Akullersuup Sermia (AS), and Narsap Sermia (NS), and three land-terminating glaciers: Qamanaarsuup Sermia (QS), Kangilinnguata Sermia (KS), and Saqqap Serima, which drains through Lake Tasersuaq (LT).
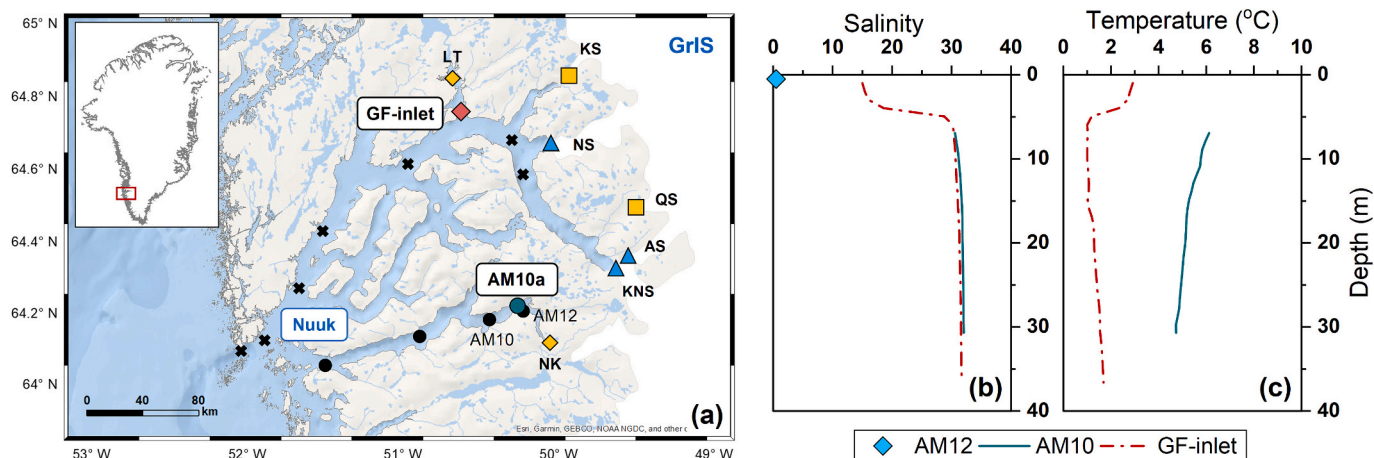
Fig. 1. Sample location and fjord hydrography on the southwest margin of Greenland. (a) Map of Ameralik Fjord and Nuup Kangerlua. The CTD stations are indicated by solid black circles and crosses in Ameralik Fjord (AM) and Nuup Kagerlua (GF), respectively, with selected stations in Ameralik Fjord annotated as AMx. The coring sites, AM10a and GF-inlet, are labeled in a green dot and red diamond, separately. Blue labels show the position of Nuuk and the Greenland Ice Sheet (GrIS). Other acronyms represent marine-terminating glaciers (NS, AS, and KNS) by blue triangles, land-terminating glaciers (KS and QS) by yellow squares, and major meltwater sources (LT and NK) by yellow diamonds. Profiles of (b) salinity and (c) temperature of overlying water column (AM12: blue diamond; AM10: green solid line; GF-inlet: red dash-dotted line). The data point at station AM12 was obtained with YSI EXO2 sensors supplied via a flow cell to an uncontaminated fjord water supply. (For interpretation of the references to colour in this figure legend, the reader is referred to the web version of this article.)

The research area is located on the North Atlantic craton of southern West Greenland, consisting predominantly of orthogneisses with tonalite-trondhjemite-granodiorite (TTG) compositions, comprising Archean metavolcanic amphibolite and anorthosite (Windley and Garde, 2009; Svahnberg, 2010). There are two different anorthosite-bearing layered intrusions near the study sites: a) the Ivisaartoq meta-volcanic (greenstone) belt, mainly comprising volcanics, with layers of gabbros, metaperidotites/serpentinites, and smaller amounts of sediments (Windley and Garde, 2009; Szilas et al., 2016; Polat et al., 2018), located between KS and NS of Nuup Kangerlua; and b) the Naajat Kuuat Anorthosite Complex, composed of anorthosites, gabbros and ultramafic rocks (Hoffmann et al., 2012), located at the head of Ameralik Fjord.

Samples were collected aboard the R/V Tulu in September 2019. The site AM10a is near the river mouth of NK in Ameralik Fjord (Fig. 1a), with a water depth of approximately 30 m. Site GF-inlet is situated in a northern inlet of Nuup Kangerlua (Fig. 1a) surrounded by mountains where the water depth is 41–42 m. Temperature, salinity, and depth profiles were recorded using a CTD (YSI EXO2 sonde) at site AM10 and site GF-inlet (Table 1). Fjordic water samples were collected using a Teflon-lined water pump attached to a bespoke-made plastic Towfish (for near surface samples only) and a standard Niskin sampling bottle (for sub surface samples), at AM10, AM12, and GF-inlet stations. Water samples for suspended sediment ASi analysis were filtered using 0.4 μm polycarbonate filters (25 mm diameter) at AM12 and GF-inlet, and the filters were sealed in foils after air drying at ambient temperature (Hawkings et al., 2017).

Sediment cores were collected by a large bore sediment corer (Aquatic Research Instruments) fitted with a polyvinyl chloride (PVC) core tube of 50 cm length and 9.5 cm diameter, and three sediment cores were collected at each sampling site (AM10a and GF-inlet). One core was extruded, sliced at 1 cm intervals, and stored in plastic bags in dark

and cool conditions. The other two cores were used for pore water sampling and core incubation experiments, respectively.

For pore water sampling, holes were drilled at 2 cm intervals on the core tube, through which 0.15 μm pore size Rhizon (Rhizosphere) samplers could be inserted into the sediment cores (Ng et al., 2020). Samples were extracted through Rhizon filters into the syringes via vacuum suction. The interface pore water was collected at 0–1 cm depth. Core-top water was extracted prior to the pore water, to reduce the risk of pore water dilution from potential down-flow of core-top water into the sediment core.

2.2. Core incubation experiment

In order to evaluate any processes contributing to benthic DSi fluxes in addition to molecular diffusion, a core incubation experiment was carried out in the GF-inlet core (10 cm diameter) following the methodology described in Hammond et al. (2004), with a magnetic stirrer set 10 cm above the sediment surface and stirring at 32 rpm to maintain constant mixing of the core-top water column, and to avoid sediment resuspension.

The core-top water was collected at selected time intervals over approximately a 24-h period (Table S1 in the SI), and filtered through 0.45 μm Acrodisc Supor syringe filters. The surrounding air temperature and the height of water column above the sediment were measured over the 24-h incubation period. Measurements showed that the air temperature varied between 0.8 °C and 5.6 °C. Due to the progressive sample collection, the water column height above the cores decreased from 28 cm to 15 cm over the 24 h (Table S1 in the SI). The core-top water samples were transferred into acid-cleaned polytetrafluoro-ethylene (PTFE) bottles with split samples frozen at −20 °C for subsequent nutrient analyses at Plymouth Marine Laboratory (UK). The

Table 1
Study site information.

Sites	Latitude	Longitude	Water depth	Bottom temperature (°C)		Bottom salinity
	°N	°E	m	In-situ	Incubation	
AM10a Ameralik Fjord	64.2182	−50.2562	30	4.73	2.9 ± 0.1	31.75
AM10 Ameralik Fjord	64.1840	−50.4324	–	–	–	–
AM12 Ameralik Fjord	64.2092	−50.2317	–	–	–	–
GF-inlet Nuup Kangerlua	64.7594	−50.6271	41–42	1.69	3.1 ± 0.6	31.34

remaining portions were kept in dark and cool conditions for subsequent Si isotope and elemental analyses, given the potential for freezing to influence Si isotopic compositions (Sutton et al., 2018b).

2.3. Scanning Electron Microscopy (SEM) and Energy Dispersive Spectroscopy (EDS)

In order to assess the ASi phase present in the sediment and sediment grain size, sediments from the sliced sediment cores were analyzed under the scanning electron microscope (SEM) at the electron microbeam laboratory within University of Bristol (UK). Sediment particles of selected depth were separated with deionized water (Milli-Q, Millipore, 18.2 MΩ), mounted, and coated with 10 nm gold coating for instrument analysis. The morphology and structure phase of silica were observed using a Hitachi S-3500 N SEM operating at 20 kV. Chemical compositions of specific particles were determined by a Thermo Noran energy dispersive spectrometer (EDS x-ray detector) equipped on the SEM.

2.4. Solid phase extraction

2.4.1. Reactive Si phases in sediments

Operationally-defined reactive Si pools in sediments were determined with a sequential leaching method following Michalopoulos and Aller (2004) and Pickering et al. (2020). Extracted reactive Si phases here include (a) mild acid-leachable silica (Si-HCl) associated with authigenic products, for example, metal oxide coatings, authigenic silicates, and some detrital clays; (b) mild-alkaline leachable amorphous silica (Si-Alk) that is mainly composed of glacially-derived ASi; (c) NaOH digested silica (Si-NaOH) associated with soluble lithogenic silica (LSi) and remaining refractory BSi (Michalopoulos and Aller, 2004; Pickering et al., 2020; Pryer et al., 2020; Ng et al., 2022; Ward et al., 2022a). Briefly, wet sediment samples were dried at 40 °C and gently homogenized. The impact of drying process on the determination of different reactive Si pools, including concentration and isotope measurements, is assessed with an additional experiment detailed in Text S1 in the SI.

Approximately 80 mg of dry sediments were accurately weighed. Samples then were treated with 36 mL of 0.1 M HCl (in-house distilled) to extract Si-HCl and to precondition the surface of ASi for subsequent alkaline dissolution (Michalopoulos and Aller, 2004; Pickering et al., 2020). The Si-HCl leachates were centrifuged and then filtered through 0.22 μm polyethersulfone (PES) filters, adjusted to pH 3, and stored for subsequent Si isotope analysis. Remaining sediments were rinsed, dried again, and digested with 5 mL of 10 % H_2O_2 solution (Romil SpA™) for 30 min to remove organic matters (Ng et al., 2022; Ward et al., 2022a; Ward et al., 2022b).

After rinsed and re-dried, these HCl- and H_2O_2- pretreated sediments were extracted through 40 mL of 0.1 M Na_2CO_3 (ACROS Organics™) in a water bath at 85 °C for 5 h to determine the Si-Alk pool (DeMaster, 1981). At the first 20 min of leaching, approximate 10 mL portion of supernatant was taken for subsequent Si isotope analysis (filtered through 0.22 μm PES filters and neutralized with HCl before instrument test), to minimize the contamination from significant LSi dissolution. Additional aliquots were also subsampled at 2 h, 3 h and 5 h to determine the content of Si-Alk quantitatively, using a fitted linear regression between measured aliquot [DSi] and associated time point following DeMaster (1981). The extrapolated intercept at 0 h was considered as the content of Si-Alk in sediments.

The residual sediments were rinsed, dried, and then treated with 10 mL 4 M NaOH (Honeywell Fluka™) in an 85 °C water bath for 2 h. After 2 h, the supernatant was removed following centrifugation and the residual sediments were rinsed 3 times using Milli-Q water (18.2 MΩ) to remove any remaining leachate. Both the supernatant and the 3-part rinses were filtered through 0.22 μm syringe PES filters, added together as NaOH leachate, neutralized with 10 N HCl (in-house distilled), and stored for further analysis.

The [DSi] of HCl, Na_2CO_3, and NaOH leachate were determined using the molybdate-blue method according to DeMaster (1981) on a VMR V-1200 Vis spectrophotometer (Ng et al., 2020; Ng et al., 2022) at the University of Bristol (UK) with an analytical error of 3 %.

2.4.2. Reactive Si phases in suspended sediments

An alkaline extraction method (Ragueneau et al., 2005; Lam et al., 2015; Hatton et al., 2019) was used to determine the content of ASi attached to glacial SPM. Suspended sediment samples preserved on 0.4 μm polycarbonate filters were placed in a fume hood in a Class 10 clean lab at room temperature (22 °C) to ensure the removal of all moisture. The dry filters were treated with 0.2 M NaOH (Honeywell Fluka™) at 100 °C on a hotplate for 1 h to leach SPM ASi. Samples were neutralized with 0.14 mL 6 M HCl (in-house distilled) immediately after the digestion period, to stop further dissolution. Following the centrifugation, the solution was filtered through 0.22 μm syringe PES filters, for Si isotope analysis and ASi concentration evaluation. The content of Si in NaOH leachate was measured at the University of Bristol (UK) by the molybdate-blue method (DeMaster, 1981) with a Hach DR3900 spectrophotometer, the analytical error of which is around 3 %.

2.5. Nutrient analysis

The concentrations of nitrate and silicic acid in pore waters and core-top waters collected from the core incubation experiment were measured using the stored frozen samples and a 5-channel segmented flow colorimetric nutrient autoanalyzer (Seal Analytical AA3) at Plymouth Marine Laboratory (UK), following the analytical methods described in Woodward and Rees (2001). The samples were analyzed along with nutrient reference materials (KANSO Technos, Japan), to confirm data quality and analytical confidence. Limits of detection for the nutrients were 0.02 μmol/L for both nitrate and silicic acid with an analytical uncertainty of 3–4 %. Sample handling and defrosting, and analytical procedures, were according to the Global Ocean Ship-based Hydrographic Investigations Program (GO-SHIP) nutrient protocols (Becker et al., 2020).

2.6. Si isotope analysis

Instrumental Si isotope analysis was carried out on processed pore water, core-top water, and leachate samples, and reference standards. The preparation processes are further described in the following subsections.

2.6.1. Sample pre-concentration and purification

Due to low [DSi] and variable salt-water matrix, pore waters and core-top waters were pre-concentrated using the Mg-induced co-precipitation method (Karl and Tien, 1992; Reynolds et al., 2006a; de Souza et al., 2012) prior to isotope analysis. The processed pore water and core-top water, filtered sediment and particle leachates, and reference standards, were purified via cation exchange chromatography following Georg et al. (2006). The Si yield of the method was found to be approximately 95 % (details are presented in Text S2 in the SI).

2.6.2. Mass spectrometry

Stable Si isotopes (^{28}Si, ^{29}Si, ^{30}Si) were measured at Bristol Isotope Group laboratory (University of Bristol, UK) using a Thermo Finnigan Neptune, multicollector-inductively coupled plasma-mass spectrometer (MC-ICP-MS). Solutions were transferred into dry plasma mode via a PFV nebulizer connected to an Apex IR Desolvating Nebulizer. Samples and standards were treated with 0.1 M H_2SO_4 (ROMIL-UpA) and 1 M HCl (in-house distilled) to counteract anionic matrix effects (SO_4^{2-} and Cl^-) (Hughes et al., 2011). All solutions were analyzed using standard-sample bracketing and Mg-doping methods to correct for instrumental mass bias and matrix effects (Cardinal et al., 2003).

Stable Si isotopic compositions are typically expressed as δ^nSi

notation in units of per mil (‰), representing a deviation of the $^{30}Si/^{28}Si$ or $^{29}Si/^{28}Si$ of the sample relative to the international standard NBS-28 (Eq. 1).

$$\delta^{n}Si = \left[\frac{\left(^{n}Si/^{28}Si\right)_{sample}}{\left(^{n}Si/^{28}Si\right)_{NBS-28}} - 1 \right] \times 1000 \tag{1}$$

The long-term external reproducibility was assessed with replicate measurements of three pre-purified Si reference standards; ALOHA$_{1000}$ seawater standard, LMG-08 sponge standard, and Diatomite rock standard. Average $\delta^{30}Si$ measurements are $+1.25 \pm 0.04$ ‰ (ALOHA$_{1000}$, $n = 11$), -3.43 ± 0.09 ‰ (LMG-08, $n = 36$), and $+1.27 \pm 0.08$ ‰ (Diatomite, $n = 29$), which are in good agreement with published values within 2 SD: $+1.24 \pm 0.20$ ‰ (Grasse et al., 2017), -3.43 ± 0.15 ‰ (Hendry and Robinson, 2012), and $+1.26 \pm 0.20$ ‰ (Reynolds et al., 2007), respectively. Replicate measurements were also made on sample solutions (n = 2–4). Reproducibility (2 SD) ranges from <0.01 ‰ to 0.19 ‰ for pore water samples ($n = 33$), 0.01 ‰ to 0.27 ‰ for core-top water samples ($n = 18$), and from <0.01 ‰ to 0.20 ‰ for solid leachates ($n = 89$). For all samples and standards, the analyzed $\delta^{29}Si$ and $\delta^{30}Si$ show a positive linear correlation through the origin. This mass-dependent fractionation line shows a slope of 0.5142 ± 0.0009 ($n = 308$), which lays in between a purely thermodynamic (0.5178) and kinetic (0.5092) mass-dependent fractionation (Reynolds et al., 2006b; Reynolds et al., 2007).

2.7. Major and trace element analysis

Prior to concentration analysis, selected split portions of pore water samples were acidified with 1 % v/v 10 M laboratory distilled HCl and left to equilibrate for 3 months. The concentrations of major elements: K and Mg, and trace elements: Li, Al, manganese (Mn), and Fe, were determined by an Agilent 8800 inductively coupled plasma-triple quadrupole-mass spectrometer (ICP-QQQ-MS) at the Open University (UK). Analytical performance was assessed through periodic measurement of blanks and synthetic in-house standards, in addition to two certified reference materials, SLRS-6 and CASS-6, which indicate a precision of better than 2.2 % and accuracy of better than 3.9 % respectively.

2.8. Benthic DSi flux calculation

Previous studies have established that Fick's First Law could only account for benthic DSi flux maintained by molecular diffusion (Schulz and Zabel, 2006). Additional contributors to benthic DSi flux, like bioturbation, bioirrigation, pore water advection, and other DSi releasing activities at the sediment-water interface, need to be examined through other methods, such as core incubation experiments and benthic landers/chambers (Hammond et al., 2004; Janssen et al., 2005).

We used two different methods to estimate the benthic DSi flux from sediments to overlying fjordic waters: (a) total flux measured directly from the core incubation experiment at GF-inlet; and (b) diffusion flux calculated from pore water DSi profiles at both the AM10a and GF-inlet sites. Over the incubation period, the [DSi] change rate in the core-top water was dependent on the ratio of DSi flux per unit area to effective core-top water column height (Hammond et al., 2004). The DSi flux derived from core incubations was reported as total benthic DSi flux, J_{total}. The core-top water [DSi] was plotted against the sum of elapsed time over water column height (Fig. 2), where the slope represented J_{total}. The associated uncertainty was derived from the standard error (SE) of the slope. This method could correct any systematic bias caused by sampling-induced water column height decrease (Hammond et al., 2004; Ng et al., 2020).

There are several methods for the calculation of molecular diffusive DSi fluxes, here, we use an exponential of the whole pore water [DSi] profile since the fitting with top few centimetres are largely influenced by data limitations. Thus, the diffusion flux of pore water DSi across the sediment-water interface was calculated from Fick's First Law of Diffusion as the following (McManus et al., 1995):

$$C_z = C_d - (C_d - C_0) \times e^{-\beta z} \tag{2}$$

where C_z is the pore water [DSi] (mmol m^{-3}) as a function of depth z (m), while C_d, C_0, and β are fitting parameters. The core-top water [DSi] is represented by C_0 (mmol m^{-3}) and β (m^{-1}) expresses the curvature of the exponential profile, reflecting the depth at which pore water [DSi] approaches asymptotic concentration, C_d (mmol m^{-3}). Then, the diffusion DSi flux through the sediment-water interface, $J_{diffusion}$, was estimated using Fick's First Law of Diffusion:

$$J_{diffusion} = -\phi_0 \bullet D_{sed} \bullet \left(\frac{\partial C}{\partial z} \right)_0 \tag{3}$$
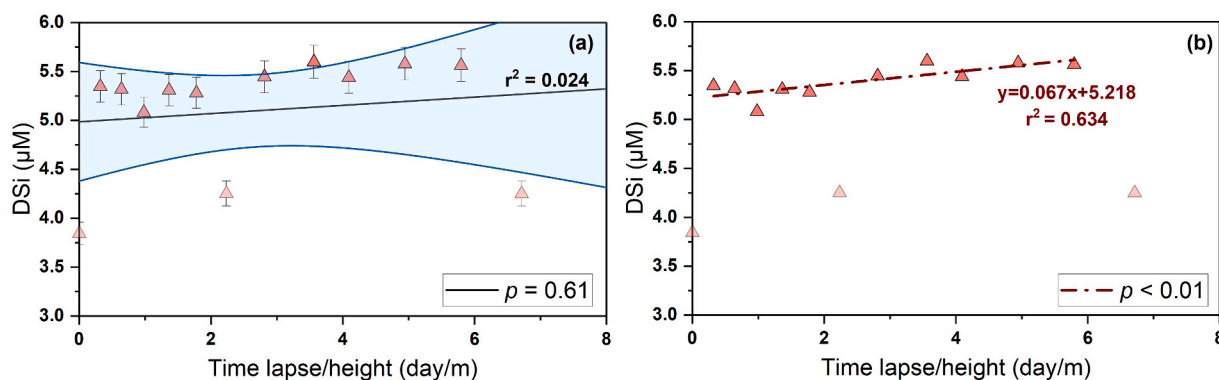
Fig. 2. Core-top water DSi concentration ([DSi]) against the ratio of incubation time and water column height at GF-inlet. (a) Outlier identification. Vertical error bars represent analytical uncertainties of [DSi] measurement. The black line represents the linear fit regression with the *p*-values of 0.61, which is greater than 0.05, indicating there is no significant correlation between [DSi] and the ratio of time lapse/height. Meanwhile, the three pale symbols are obviously out of the 95 % confidence interval (blue lines). It is thus likely that these three data are outliers for fitting analysis. (b) Total flux calculation without outliers. Dash-dot line shows new linear fit regression without pale-symbol-denote outliers (*p* < 0.01). New calculated statistically significant p-value and increased r-square value from 0.024 to 0.634 support the hypothesis above, providing strong evidence for the existence of correlation between core-top water [DSi] and time lapse/height. Therefore, we suggest that the flux calculation of this non-outlier linear model is valid. Total benthic fluxes are expressed as the slope of the regression line. (For interpretation of the references to colour in this figure legend, the reader is referred to the web version of this article.)

$$D_{sed} = \frac{D_{sw}}{\theta^2} \qquad (4)$$

$$\theta^2 = 1 - ln(\phi^2) \qquad (5)$$

where φ_0 is the porosity of sediments at 0–1 cm depth; D_{sed} is the diffusion coefficient of DSi corrected for tortuosity (Boudreau, 1996) (Eq. 4), D_{sw} is the diffusion coefficient of DSi in seawater at in-situ temperature (Table 1) (Rebreanu et al., 2008), θ is the tortuosity, and $\left(\frac{\partial C}{\partial z}\right)_0$ is the concentration gradient at the sediment-water interface (z = 0). Parameter values and associated standard errors are listed in Table 2 and Table 3 separately. Uncertainties are propagated to the final calculated values of diffusive flux.

3. Results

3.1. Dissolved Si concentration and Si isotope composition in pore water profiles

Pore water [DSi] generally increases with depth from bottom water column values of 3.02 μM and 12.46 μM reaching maximum average pore water [DSi] of 93 μM and 198 μM for AM10a and GF-inlet, respectively (Fig. 3a and d).

The isotopic compositions of DSi (denoted by $\delta^{30}Si_{DSi}$) measured in pore water (expressed as $\delta^{30}Si_{DSi-pw}$) is overall higher than those collected at the bottom of the water column (expressed as $\delta^{30}Si_{DSi-ctw}$) at AM10a (Fig. 3a) and GF-inlet (Fig. 3d). Pore water DSi $\delta^{30}Si$ values range from +1.68 ‰ and + 2.24 ‰ at AM10a (Fig. 3a) and from +0.80 ‰ to +2.33 ‰ at GF-inlet (Fig. 3d). The downcore isotopic trends differ even more significantly between the locations. Pore water $\delta^{30}Si_{DSi}$ at site AM10a exhibits generally slight fluctuations, except an increase from +1.81 ‰ at 12 cm to +2.24 ‰ at 14 cm, followed by a decrease from +2.24 ‰ at 14 cm to +1.81 ‰ at 22 cm (Fig. 3a). The GF-inlet pore water profile is more variable, with $\delta^{30}Si_{DSi}$ increasing sharply from +0.80 ‰ to 1.70 ‰ within the top 2 cm, and then varying downcore between +1.80 ‰ and + 2.33 ‰ (Fig. 3d).

3.2. Sediment composition

Both AM10a and GF-inlet are characterized by silt and an absence of diatoms or sponge spicules in the sediment composition (Fig. S2 in the SI). The grain size of particles at AM10a mainly range between 5 μm and 20 μm (Fig. S2a in the SI), generally coarser than sediment at GF-inlet, where grain size mainly ranges between 5 and 10 μm (Fig. S2d in the SI). SEM images of these sediments support the absence of biogenic silica, and show poorly-structured sediment coatings that are characterized by large Si and O peaks in the EDS spectra and lack clear evidence of crystallinity, which we assume dominates the Si-Alk pool, lacks crystallinity (Figs. S2b,c and S2e,f in the SI).

3.3. Content and isotopic composition of reactive solid Si phases

The content of Si-Alk at AM10a varies between 97.8 μmol/g and 277.8 μmol/g, with a general decrease from 211.3 μmol/g to 114.0 μmol/g in the top 8 cm and a gradual increase below 15 cm (Fig. 3b). The Si-Alk content data at GF-inlet vary between 119.2 μmol/g and 256.9 μmol/g (Fig. 3e). Both sites reach Si-Alk content peaks at 10 cm below the sediment surface.

The isotope values of Si-Alk (denoted by $\delta^{30}Si_{Alk}$) at AM10a shows higher variability in the top section of the core (from 0 cm to 12 cm); then $\delta^{30}Si_{Alk}$ stabilizes at around +0.76 ‰, except for a peak that centered at around 25 cm (Fig. 3b). Meanwhile, the Si-Alk $\delta^{30}Si$ values at GF-inlet are relatively constant, with an average of +1.07 ± 0.29 ‰ (2 SD, $n = 11$) (Fig. 3e). The isotopic composition of the Si-HCl pool ($\delta^{30}Si_{HCl}$) is much lighter than those of the Si-Alk pool. The $\delta^{30}Si_{HCl}$ data at AM10a are variable, averaging at −1.14 ± 0.07 ‰ (2 SD, $n = 40$) (Fig. 3c), while the $\delta^{30}Si_{HCl}$ data at GF-inlet generally exhibit a decreasing trend with depth (Pearson's $r = −0.79$, $p < 0.01$), with an average of −1.03 ± 0.10 ‰ (2 SD, n = 11) (Fig. 3f). Compared with Si-HCl pool and Si-Alk pool, SPM ASi is characterized by an isotopic composition (denoted by $\delta^{30}Si_{ASi-APM}$) between $\delta^{30}Si_{HCl}$ and $\delta^{30}Si_{Alk}$, with $\delta^{30}Si$ values of +0.69 ‰ at AM10a (Fig. 3b) and −0.05 ‰ at GF-

Table 3
Uncertainty evaluation in $J_{diffusion}$ calculation.

Site	SE (φ_0)	SE (D_{sw})	SE (θ^2)	SE (β)	SE (C_0)	SE (C_d)	SE ($J_{diffusion}$)
		m^2 day^{-1}		m^{-1}	mmol m^{-3}	mmol m^{-3}	mmol m^{-2} day^{-1}
AM10a	0.003	8.7×10^{-7}	0.010	9.328	0.091	5.332	0.015
GF-inlet	0.000	7.5×10^{-7}	0.001	1.101	0.115	59.235	0.011

Note: Relative uncertainty, R, is defined as the ratio of standard error (SE) and original value, e.g. $R(\varphi_0) = \frac{SE(\phi_0)}{\phi_0}$. The relative uncertainty of $J_{diffusion}$ is the sum of the relative uncertainty associated with each parameter in the following formulae: $R(J_{diffusion}) = R(\varphi_0) + R(D_{sw}) + R(\theta^2) + R(\beta) + R(C_d—C_0)$, i.e. $R(J_{diffusion}) = \frac{SE(\phi_0)}{\phi_0} + \frac{SE(D_{sw})}{D_{sw}} + \frac{SE(\theta^2)}{\theta^2} + \frac{SE(\beta)}{\beta} + \frac{SE(C_d) + SE(C_0)}{C_d - C_0}$. The absolute uncertainty of $J_{diffusion}$ is the product of relative uncertainty $R(J_{diffusion})$ and calculated values $J_{diffusion}$.

Table 2
Parameters used to calculate diffusion DSi flux, $J_{diffusion}$, at the sediment-water.

Site	$\varphi_0^{(a)}$	$D_{sw}^{(b)}$	θ^2	$\beta^{(c)}$	$C_0^{(d)}$	$C_d^{(c)}$	$J_{diffusion}$
		m^2 day^{-1}		m^{-1}	mmol m^{-3}	mmol m^{-3}	mmol m^{-2} day^{-1}
AM10a	0.605	4.598×10^{-5}	2.006	30.468	3.023	93.554	0.038
GF-inlet	0.840	3.960×10^{-5}	1.349	2.753	3.843	237.180	0.016

Definition: φ_0 – sediment porosity at 0–1 cm depth; D_{sw} – diffusion coefficient of silicic acid in seawater at in-situ temperature; θ – tortuosity; β – expresses the inverse of the profile scale length; C_0 – core-top water DSi concentration; C_d – asymptotic pore water DSi concentration.

(a) The porosity φ_0 was determined from weight measurement of 0-1 cm sediment following Schulz and Zabel, 2006 (Schulz and Zabel, 2006), using the formula: $\varphi_0 = \frac{Pore\ water\ volume}{Total\ sediment\ volume}$. Volume is the ratio of mass and density. Sediment mass was measured directly using a balance with an analytical error of 0.0001 g and density values of 1.025 g cm^{-3} and 1.5 g cm^{-3} were assumed for pore water and sediment respectively.

(b) Estimation of temperature-dependent D_{sw} was based on a linear regression of previous experiment results of sea water samples at different temperatures (Rebreanu et al., 2008). The in-situ bottom water temperatures were shown in Table 1 and uncertainties were calculated from the standard errors of the slope and the intercept.

(c) Both β and C_d were determined from exponential fit of pore water DSi profiles (Fig. 3a and d) using Eq. 2. Associated uncertainties were determined as standard errors of exponential expressions using the Dynamic Fit Wizard function in SigmaPlot (Systat Software Inc.).

(d) The core-top water DSi concentration, C_0, was measured separately in AM10a and at the beginning of core incubation experiment in GF-inlet. The analytical error was 3 %.
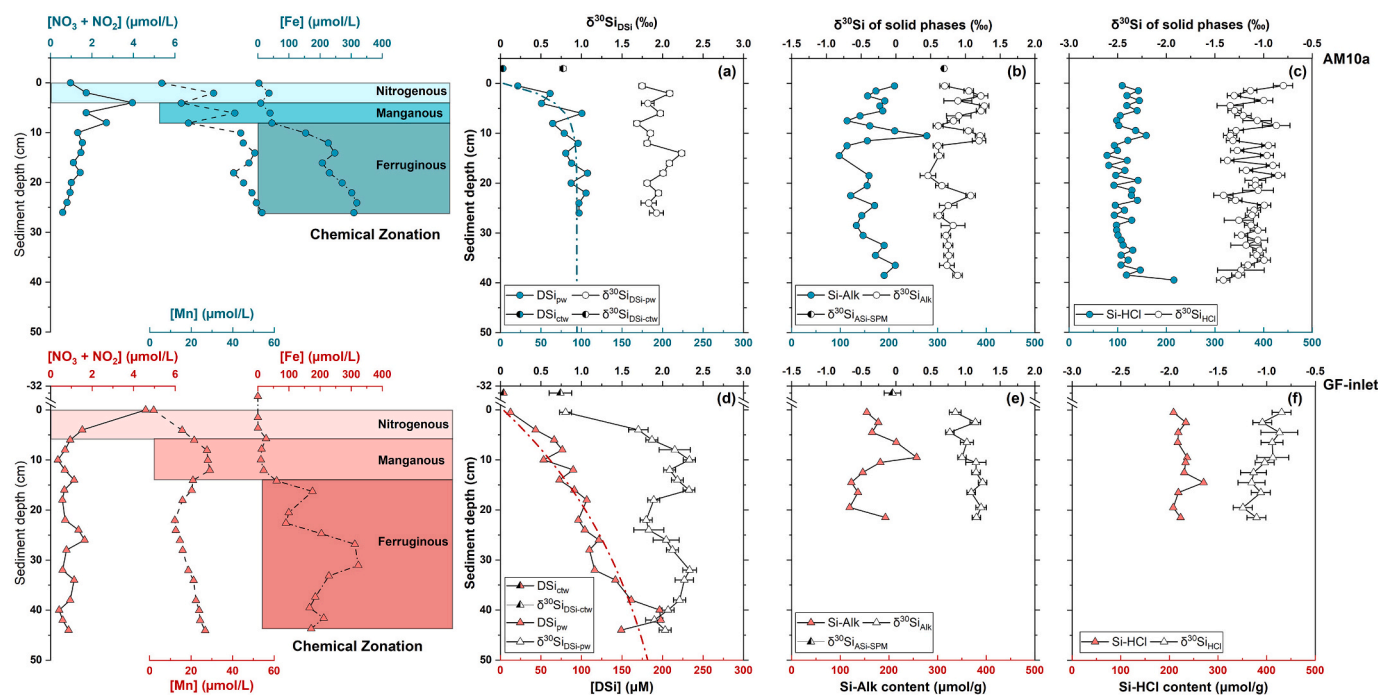
Fig. 3. Silicon contents and isotope compositions of different Si phases. (a) silicic acid concentration ([DSi]) and isotope values ($\delta^{30}Si_{DSi}$) in pore water ($\delta^{30}Si_{DSi-pw}$) and core-top water ($\delta^{30}Si_{DSi-ctw}$) at AM10a; (b) content of sediment amorphous silica (Si-Alk) and Si isotopic compositions of sediment amorphous silica ($\delta^{30}Si_{Alk}$), suspended sediment amorphous silica ($\delta^{30}Si_{ASi-SPM}$) at AM10a; (c) content and isotopic composition of HCl-leachable silica (Si-HCl, $\delta^{30}Si_{HCl}$) at AM10a; (d) silicic acid concentration ([DSi]) and isotope values ($\delta^{30}Si_{DSi}$) in pore water ($\delta^{30}Si_{DSi-pw}$) and core-top water ($\delta^{30}Si_{DSi-ctw}$) at GF-inlet; (e) content of sediment amorphous silica (Si-Alk) and Si isotopic compositions of sediment amorphous silica ($\delta^{30}Si_{Alk}$), suspended sediment amorphous silica ($\delta^{30}Si_{ASi-SPM}$); (f) content and isotopic composition of HCl-leachable silica (Si-HCl, $\delta^{30}Si_{HCl}$) at GF-inlet. The dash-dot curves in DSi profiles (a) and (e) indicate the exponential fitting line of concentration and depth. Core-top data point of AM10a corresponds to seawater sampled 3 cm above sediment. Core-top data point at GF-inlet indicates the core-top water collected at the beginning of the core incubation experiment. Horizontal error bars represent 2 SD of repeated $\delta^{30}Si$ measurements ($n = 2$–4). Error bars not indicated are within symbol size. Chemical zonations are determined from the concentrations of pore water dissolved nitrate + nitrite, manganese, and iron, displayed on the left (concentration profiles are also shown in Fig. 4).

inlet (Fig. 3e), respectively.

3.4. Pore water chemistry

The GF-inlet core results show the strongest increase in both dissolved potassium (K) (Fig. 4a) and magnesium (Mg) (Fig. 4b) concentrations (indicated by [K] and [Mg], respectively) within the upper 8 cm profile depth, and similar to the trend observed in the isotopic composition of pore water DSi, below which the increasing gradient declines until reaching asymptotic values. Both AM10a and GF-inlet cores exhibit similar and relatively constant values in pore water [Mg], except at the interface (Fig. 4a and b).

Pore water lithium (Li) concentrations ([Li]) (Fig. 4c) at AM10a are more variable in the top section of the core; below 12 cm pore water [Li] stabilizes at around 14 μM. Meanwhile, a significant decrease of pore water [Li] is observed in the uppermost 14 cm at GF-inlet, whereas below this depth, [Li] increases continuously and approaches 15 μM, close to the interface value. Measurements show negative correlations between [Li] and $\delta^{30}Si_{DSi-pw}$ at both AM10a (Fig. 4h, Pearson's $r = -0.93$, $p < 0.001$) and GF-inlet (Fig. 4i, Pearson's $r = -0.66$, $p < 0.01$).

The core AM10a exhibits two pronounced peaks in aluminium (Al) concentrations ([Al]) (Fig. 4d) of around 30 μM at 12–14 cm and 40 μM at 22 cm. At GF-inlet, pore water [Al] varies from 12 μM to almost 30 μM from 0 cm to 12 cm, then stabilizes at around 16 μM until 26 cm, followed by two small peaks at 32 cm and 42 cm to 15 μM and 30 μM, respectively.

At the AM10a site, pore water nitrate + nitrite (NO₃ + NO₂) concentrations ([NO₃ + NO₂]) are more variable in the top 10 cm of the core, and then gradually decrease down to 0.59 μM deeper down the core (Fig. 4e), while Mn concentrations ([Mn]) show a general downcore

increase up to 54 μM (Fig. 4f). At the GF-inlet site, pore water [Mn] is elevated relative to the interface (0 cm) (Fig. 4e), while pore water [NO₃ + NO₂] is reduced relative to the interface (Fig. 4f). Dissolved Fe concentrations ([Fe]) remain low within the uppermost 8 cm at AM10a and 14 cm at GF-inlet, which then increase sharply to 247 μM for AM10a and to 176 μM for GF-inlet, respectively (Fig. 4g).

3.5. Benthic DSi flux

Total DSi flux (J_{total}) was calculated from the core incubation profiles of DSi and the ratio of time lapse and water column height (Fig. 2) at GF-inlet. The relatively linear trend in Fig. 2b suggests that the benthic DSi flux was almost constant at the GF-inlet site throughout the experiment. Calculated J_{total} is around 0.067 ± 0.018 mmol m^{-2} day^{-1} (Fig. 2b). We note that the discrepancy of temperature between the in-situ (fjord bottom) and the core incubation environment (Table 1) may introduce a systematic temperature artifact for the DSi flux (Hammond et al., 2004), which may add uncertainties of 0.006 ± 0.004 mmol m^{-2} day^{-1}.

The diffusive benthic DSi fluxes, denoted by $J_{diffusion}$, are estimated from Fick's first law of diffusion. The site AM10a displays a higher $J_{diffusion}$ of 0.038 ± 0.015 mmol m^{-2} day^{-1} than the $J_{diffusion}$ observed at GF-inlet site of 0.016 ± 0.011 mmol m^{-2} day^{-1} (Table 2 and Table 3). The molecular diffusion DSi flux makes up nearly a quarter of the total benthic DSi flux at GF-inlet.
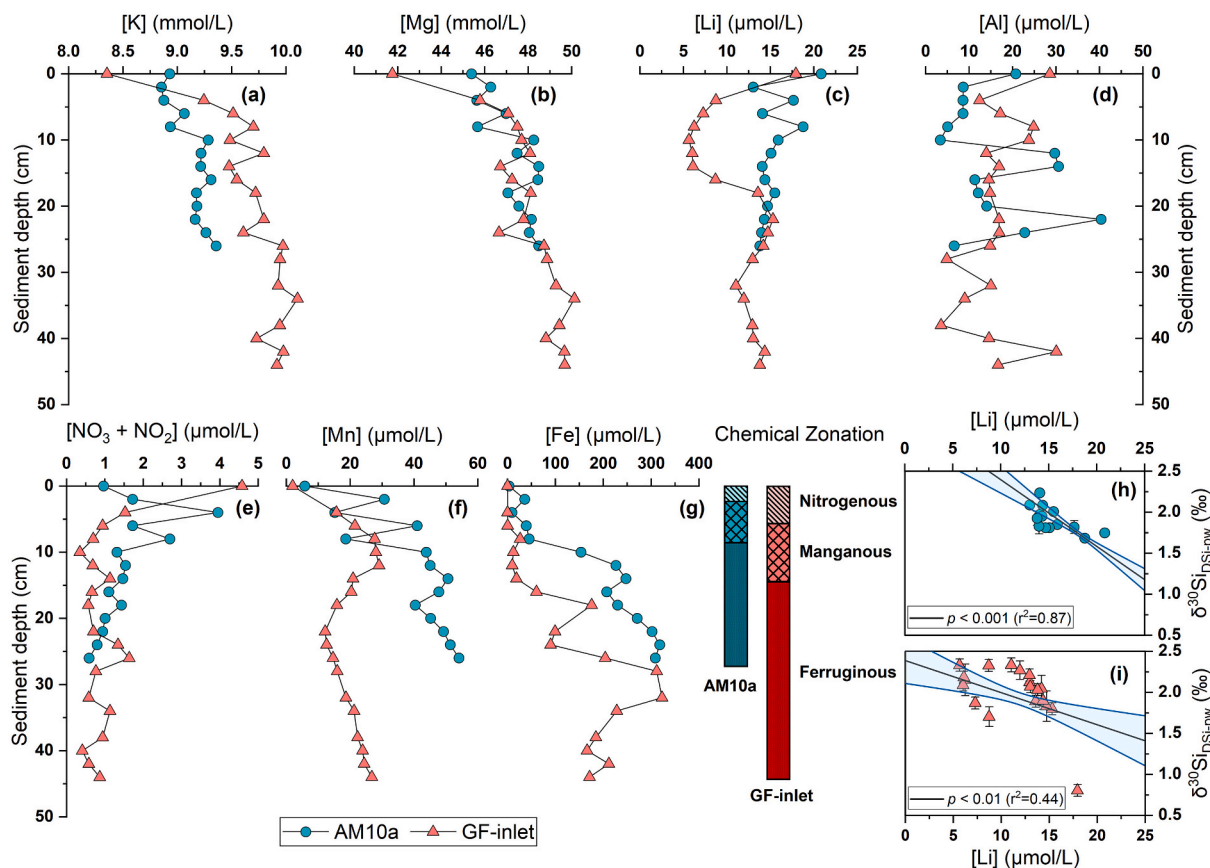
Fig. 4. Downcore concentration profiles of dissolved elements and nutrients: (a) potassium, (b) magnesium, (c) lithium, (d) aluminium, (e) nitrate + nitrite, (f) manganese, and (g) iron. A schematic interpretation of the chemical zonation, mainly determined from the pore water concentrations of nitrate + nitrite, manganese, and iron (Aller, 2014), at each site is presented alongside these data. Linear regression of pore water Li concentration ([Li]) against pore water dissolved silicon isotopic compositions ($\delta^{30}Si_{DSi-pw}$) at (h) AM10a and (i) GF-inlet. Black lines indicate the best fit linear regression and blue lines represent the 95 % confidence interval. The corresponding *p* value and r-square value of each regression line are shown on the plot. (For interpretation of the references to colour in this figure legend, the reader is referred to the web version of this article.)

4. Discussion

4.1. Sources and processes regulating pore water DSi

4.1.1. Dissolution of sediment Si-Alk

There is little evidence for the presence of diatom frustules and sponge spicules (i.e., BSi) in the sediments at two fjordic sites (Fig. S2 in the SI). Previous studies have demonstrated that submarine weathering and dissolution of refractory lithogenic minerals could serve as a source of DSi in marine sediments (Geilert et al., 2020a; Ward et al., 2022a). However, given the relatively low Si-NaOH content and lower Si-NaOH to Si-Alk ratio at our study sites (Table 4), we think that the dissolution of these refractory lithogenic silicates is not as reactive as other locations, and therefore does not contribute significantly to the pore water silicic acid build-up in these glacial marine sediments. Therefore, the dominant source of pore water DSi at the study sites is most likely the soluble abiogenic ASi present in these glacial marine deposits (Fig. S2 in the SI). In addition to the dissolution of the Si-Alk phases, Si previously bonded to metal oxides might be released during their reductive dissolution, especially in these Fe-rich glacial marine sediments (Ng et al., 2020; Ng et al., 2022) (Fig. 5a).

Pore waters at both fjord sites are undersaturated with respect to silica, as the DSi concentrations are much lower than the solubility of amorphous silica at deep-sea temperatures (1000 μM) (Tréguer et al., 1995; Loucaides et al., 2012). The trends broadly follow the general asymptotic DSi concentration profiles that often characterize marine sediments (Aller, 2014) (Fig. 3a and d). Therefore, sediment Si-Alk

Table 4
Comparison between the content of sediment Si-Alk and Si-NaOH in different marine environments.

Location	Si-Alk content	Si-NaOH content	Si-NaOH/ Si-Alk	Reference
	wt%	wt%	wt%/wt%	
Ameralik Fjord	0.25–0.33	0.27–0.28	0.9–1.1	This study
Nuup Kangerlua	0.49–0.50	0.37–0.38	0.7–0.8	(Ward et al., 2022a; Ward et al., 2022b)
Arctic Barents Sea	0.17–0.52	1.12–1.34	2.6–6.7	(Ward et al., 2022a; Ward et al., 2022b)
Gulf of Mexico	0.19–0.39	1.49–3.64	5.9–14.8	(Pickering et al., 2020)

Note: The Si-Alk pool is mainly composed of amorphous silica while Si-NaOH refers to more crystallized Si phases like with soluble lithogenic silica (LSi) and remaining refractory BSi (Michalopoulos and Aller, 2004; Pickering et al., 2020; Pryer et al., 2020; Ng et al., 2022; Ward et al., 2022a).

dissolution and pore water DSi remobilization to the overlying bottom fjord waters are most effective in the surface layer, where the degree of Si undersaturation is highest (Van Cappellen and Qiu, 1997; Geilert et al., 2020a).

The isotopic compositions of the Si-Alk pool (varying between +0.86 ‰ and + 1.07 ‰) are almost within the range of previously published $\delta^{30}Si_{Alk}$ values in Arctic marine sediments under the condition of Arctic
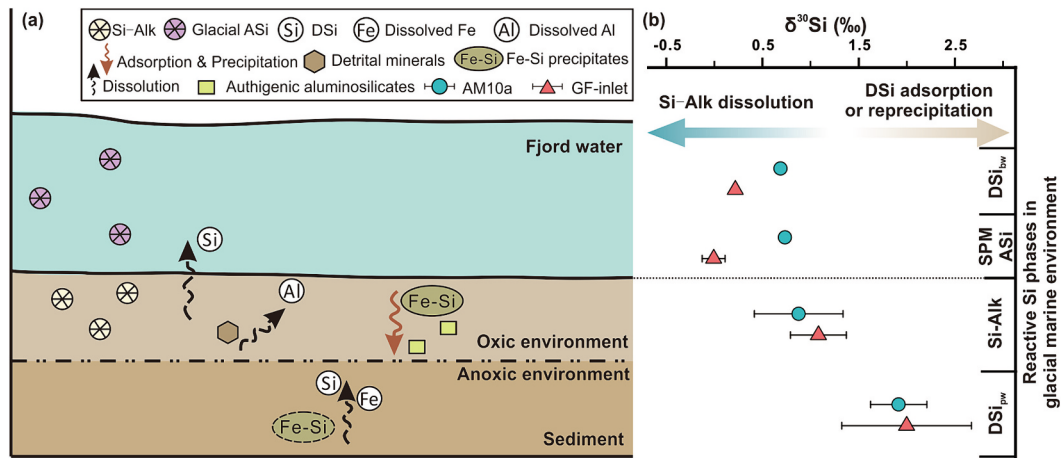
Fig. 5. (a) Schematic figure of processes controlling pore water DSi accumulation in fjord sediments. (b) The average δ^{30}Si values of different reactive Si phases in glacial marine environment, including pore water dissolved silicon (DSi$_{pw}$), bottom water dissolved silicon (DSi$_{bw}$), sediment amorphous silica (Si-Alk), and water column suspended particulate amorphous silica (SPM ASi). Horizontal error bars represent 2 SD of repeat δ^{30}Si measurements ($n = 2$) for SPM ASi and DSi$_{bw}$, and 2 SD of all downcore δ^{30}Si measurements for DSi$_{pw}$ and Si-Alk. Error bars not indicated are within symbol size. Green and brown arrows present the impact on pore water DSi isotopic compositions from different early diagenetic processes. For example, the dissolution of Si-Alk would shift pore water DSi δ^{30}Si values to more negative side while DSi adsorption and reprecipitation reactions would leave positive deviation to δ^{30}Si$_{DSi-pw}$ data. (For interpretation of the references to colour in this figure legend, the reader is referred to the web version of this article.)

Water mass ($+0.82 \pm 0.16$ ‰) (Ward et al., 2022a), but higher than the Si isotopic compositions of glacially-derived ASi (from -0.47 ‰ to -0.22 ‰) (Hawkings et al., 2018b; Hatton et al., 2019). These observations indicate that sediment Si-Alk at the fjord sites contains other ^{30}Si enriched phases in addition to the glacier-sourced ASi.

4.1.2. Diagenetic processes modifying pore water δ^{30}Si within shallow sediments

As the isotopic fractionations between the sediment Si-Alk pool and the pore water DSi pool are around -1.05 ‰ and -0.93 ‰ at AM10a and GF-inlet, respectively, the dissolution of Si-Alk pool should introduce a lower δ^{30}Si signal into the surrounding pore waters (Fig. 5b). However, such a decrease in pore water δ^{30}Si has not been observed in these two cores (Fig. 3a and d). A likely explanation is that other early diagenetic processes take place relatively early in the shallow sediments, for example, authigenic aluminosilicate precipitation and Si adsorption onto Fe oxy-hydroxides (Fig. 5a) which would introduce a higher δ^{30}Si signal to the pore waters (Ehlert et al., 2016; Geilert et al., 2020a; Ng et al., 2020; Closset et al., 2022; Ng et al., 2022; Ward et al., 2022a). These Si uptake processes might also be responsible for the high δ^{30}Si$_{DSi-pw}$ relative to δ^{30}Si$_{Alk}$ values, despite Si-Alk dissolution being the main supply of pore water DSi.

A mixing model has been previously employed (Geilert et al., 2020a; Closset et al., 2022; Ng et al., 2022; Ward et al., 2022a) to identify if other diagenetic processes are present at the sediment-water interface or within shallow sediments, in addition to the dissolution of Si-Alk. Here, we use the core-top water and fluids originating from Si-Alk dissolution as two endmembers to calculate the mixing within shallow sediments using the following equation (Geilert et al., 2020a; Closset et al., 2022; Ng et al., 2022; Ward et al., 2022a):

$$\delta^{30}Si_{mix} = \frac{\left(\delta^{30}Si_{core-top} \bullet [Si]_{core-top} \bullet f\right) + \left(\delta^{30}Si_{Alk} \bullet [Si]_{Alk} \bullet (1-f)\right)}{\left([Si]_{core-top} \bullet f\right) + \left([Si]_{Alk} \bullet (1-f)\right)} \quad (6)$$

where δ^{30}Si$_{core-top}$ and [Si]$_{core-top}$ indicates the Si isotope composition and concentration of core-top water respectively; δ^{30}Si$_{Alk}$ is the averaged δ^{30}Si in the Si-Alk pool at each site; and [Si]$_{Alk}$ expresses the equilibrium concentration in respect to Si-Alk dissolution from experimental study. We assume an equilibrium concentration of 1000 μM given the bottom water temperatures and pressures at our locations (Van

Cappellen and Qiu, 1997; Dixit et al., 2001; Rickert et al., 2002). The f value represents the proportion of core top waters for any given mixture.

Former studies have confirmed that the pore water DSi concentrations and isotopic compositions are affected by the mixing of core-top water DSi, the formation of authigenic aluminosilicates, and the interaction with Fe redox cycling (Aller, 2014; Ehlert et al., 2016; Cassarino et al., 2020; Geilert et al., 2020a; Ng et al., 2020; Ng et al., 2022; Ward et al., 2022a). If dissolution of Si-Alk is the sole diagenetic process controlling Si concentration and isotopic composition, the pore water data should fall on the mixing lines between the following two endmembers: sediment Si-Alk and core-top water DSi. Instead, both sites have heavier δ^{30}Si$_{pw}$ values (Figs. 5b and 6), likely associated with DSi re-precipitation into solid phases, which preferentially incorporates the light ^{28}Si isotope, resulting in a heavier isotopic Si composition in the remaining pore water (Ehlert et al., 2016). The Si-HCl pool includes these ^{28}Si-enriched solid phases as dilute HCl can dissolve poorly crystalline metal oxides and authigenic silicates (Michalopoulos and Aller, 2004; Pickering et al., 2020; Ng et al., 2022; Ward et al., 2022a; Ward et al., 2022b). The observed difference in isotopic composition between the Si-HCl pool and pore water DSi at our study sites are around -3 ‰. This difference is most likely a result of isotopic fractionation (Δ^{30}Si$_{solid-aqueous}$) caused by multiple precipitation processes including the formation of authigenic aluminosilicates (-2 ‰) (Ehlert et al., 2016), adsorption of DSi from pore water onto the surface of Fe oxy-hydroxides (up to -0.8 ‰ in Δ^{29}Si and up to -1.6 ‰ in Δ^{30}Si) (Delstanche et al., 2009), and amorphous Fe—Si phase co-precipitation (up to -3.2 ‰) (Zheng et al., 2016).

4.1.3. An isotopically light source of DSi

The DSi isotopic composition observed at the GF-inlet interface (pore water collected at 0–1 cm core depth) (δ^{30}Si$_{int}$) is much lighter than that of other pore waters (Fig. 6b). Natural contamination of core-top water is one potential explanation for the relatively lighter δ^{30}Si$_{int}$ value at GF-inlet. Here, we explore this possibility by considering mixing between endmembers: the core-top water and shallow pore water, the pore water collected at 2 cm depth for AM10a and 4 cm depth for GF-inlet due to sample limits, represent two endmembers and the interface represents the intermediate reservoir (Cassarino et al., 2020). The mixing line between two endmembers at GF-inlet is indicated by dash-dot line in Fig. 6b, with the interface data lying below the line. In this condition, mixing between these endmembers cannot account for the low δ^{30}Si
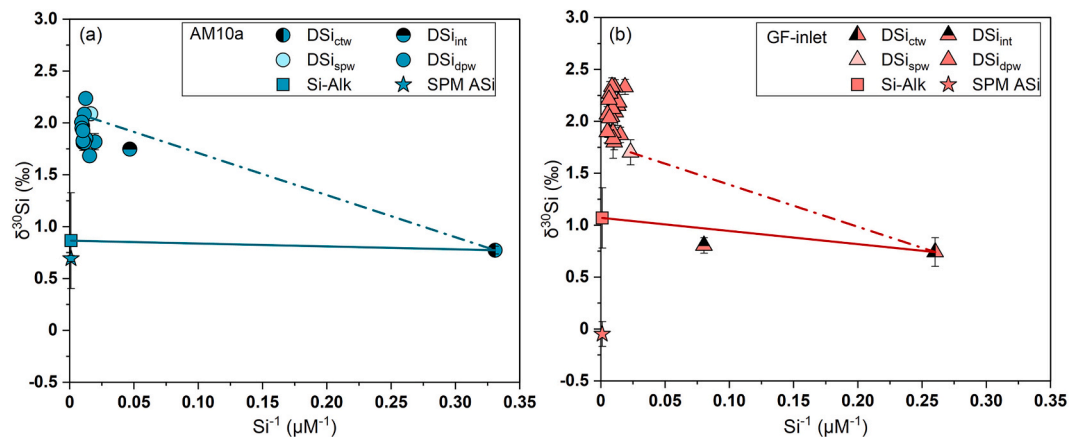
Fig. 6. Si isotope values (δ^{30}Si) are displayed against the inverse of Si concentration (Si^{-1}) for core-top water dissolved silicon (DSi$_{ctw}$), interface dissolved silicon (DSi$_{int}$), pore water dissolved silicon (DSi$_{pw}$, including shallow pore water dissolved silicon: DSi$_{spw}$ and deep water dissolved silicon: DSi$_{dpw}$), sedimentary amorphous silica (Si-Alk), and core-top water suspended sediment ASi (SPM ASi) at **(a)** AM10a and **(b)** GF-inlet. The core-top data point of AM10a corresponds to seawater sampled 3 cm above sediment, whereas the core-top data point at GF-inlet indicates the core-top water collected at the beginning of the core incubation experiment. Interface pore water indicates pore water collected at 0 cm (sediment surface). Shallow pore water refers to pore water collected at the upper 2 cm depth for AM10a and 4 cm for GF-inlet due to sample limits, with the remaining pore water defined as deep pore water (Reservoir details are presented in Fig. S3 in the SI). Vertical error bars represent 2 SD of repeat δ^{30}Si measurements ($n = 2$–4) except the error bars of Si-Alk, which indicate 2 SD of all measured downcore δ^{30}Si$_{Alk}$ values. Error bars not visible are within symbol size. The solid lines indicate the mixing lines calculated from eq. 6 according to Geilert et al. (2020a), using core-top water DSi concentration and isotope values together with the average Si-Alk content and δ^{30}Si$_{Alk}$ value of each site. The dot-dash lines represent the mixing line between two endmembers: core-top water and shallow pore water. Conservative mixing is implied if the data point falls on the linear mixing line between the endmembers, and a deviation from linearity indicates the release or uptake of Si to or from interface waters.

value at the sediment-water interface. As such, there needs to be another source to provide isotopically light Si at the surface of fjordic sediments, such as Si-Alk in surficial sediments and ASi attached to glacial SPM in water column. As the interface data also lies below the mixing line between Si-Alk and core-top water DSi (Fig. 6b, calculations are adapted from Geilert et al. (2020a)), the most likely source of the isotopically light DSi responsible for the interface observation is SPM ASi in water column, which has a measured δ^{30}Si value of -0.05 ± 0.12 ‰ (2 SD). The inferred glacial SPM ASi dissolution might only be sufficiently rapid – relative to precipitation – in the shallow sediments, such that it can leave an imprint on the interface water δ^{30}Si value.

Although two different methods were employed to extract sediment Si-Alk and water column SPM ASi, consistent results of Si isotopic compositions had been confirmed in previous publications (Hawkings et al., 2018b; Hatton et al., 2019). The higher value of δ^{30}Si$_{Alk}$ relative to δ^{30}Si$_{ASi-SPM}$ observed at the GF-inlet site is most likely due to the presence of authigenic submarine weathering products in the sediment Si-Alk pool. The water column SPM ASi collected from the study sites are expected to be mainly composed of glacially-derived ASi, given the lack of diatoms found in the underlying sediments, and the proximity to glacial runoff. However, the measured δ^{30}Si$_{ASi-SPM}$ values (AM10a: $+0.69 \pm 0.03$ ‰, GF-inlet: -0.05 ± 0.12 ‰) are higher than the previously published Si isotopic compositions of ASi attached to fine-grained SPM in bulk meltwater runoff from Greenland glacier catchments, which range from -0.47 ‰ to -0.22 ‰ (Hawkings et al., 2018b; Hatton et al., 2019). The higher values of δ^{30}Si$_{ASi-SPM}$ found in this study might imply that glacier-sourced ASi has a broader range of δ^{30}Si values than previously thought.

4.2. Ambient conditions influencing Si mobility in fjord sediments

4.2.1. Dissolution of terrigenous mineral phases and reverse weathering

The dissolution kinetics of amorphous silica can be regulated by the dissolution of terrigenous minerals through the incorporation of metals, like Al^{3+}, Fe^{2+}, and Mg^{2+} (Van Cappellen et al., 2002; Aller, 2014), and the formation of authigenic aluminosilicates (Michalopoulos and Aller, 2004; Ehlert et al., 2016). Peaks of pore water [Al] observed at the core-tops of both sites (Fig. 4d) may enhance incorporation of dissolved Al

into sediment ASi structure and precipitation of aluminosilicates (Van Cappellen and Qiu, 1997; Dixit et al., 2001; Ehlert et al., 2012; Aller, 2014). Such Al incorporation lowers the dissolution rate of ASi (Dixit et al., 2001), thus rapidly reducing DSi release into surrounding pore waters, consistent with the reduction in the downcore DSi concentration increasing rate at the Al-peak depth (Figs. 3a, d and 4d). A previous study has revealed that – due to this form of uptake – ASi solubility drops to near 600 µM (Van Cappellen et al., 2002), which is still significantly higher than pore water DSi concentrations at our study sites and unlikely to account for the asymptotic concentrations of our pore water DSi profiles (Fig. 3a and d). Therefore, the structural Al incorporation has an impact on DSi build-up in pore waters, but it is not the only process that governs the asymptotic pore water DSi concentration at our field locations.

Our downcore trends in Li provide additional insight into authigenic mineral formation. Previous studies have demonstrated that Li uptake in marine sediments is largely controlled by incorporation into authigenic clays (Martin et al., 1991; Andrews et al., 2020; Schlesinger et al., 2021), rather than being sorbed onto surfaces or being associated with metallic oxides/hydroxides (Jiang et al., 2007). As such, the observation of overall down-core decreases in pore water [Li] at both AM10a and GF-inlet (Fig. 4c) provides supporting evidence for the presence of this Li-consuming process at our study sites (Aller, 2014; Rahman, 2019). Reverse weathering also shows preferential removal of light ^{28}Si into authigenic aluminosilicates, resulting in increasing δ^{30}Si values in the remaining pore water DSi pool (Rahman, 2019; Cassarino et al., 2020). The combined impact of Li^+ consumption and light ^{28}Si uptake could explain the negative correlations between pore water Li concentration and Si isotopes that are observed at both fjordic sites (Fig. 4h and i). However, for other two other elements also associated with reverse weathering, K and Mg, there is a general increasing trend in their pore water concentrations with depth (Fig. 4a and b). Seasonal meltwater changes might be one possible reason for these changes in [K] and [Mg]. However, our study sites are deeper than 30 m, so they are below the surface water layer which is largely influenced by seasonal freshwater input (Mortensen et al., 2011; Stuart-Lee et al., 2021). Our salinity data also show similarity between summer and winter measurements: 33 in July vs 32 in September at both sites with a difference of approximately

3 %, which is relatively negligible from beginning to the end of the melt season, and unlikely takes the responsibility for concentration changes of K and Mg, especially for K at GF-inlet where the variation is over 19 % (8.4 mmol/L to 10.1 mmol/L). Therefore, the increases here are not associated with seasonal inputs, but instead could relate to other cation-release processes, such as the dissolution of terrigenous minerals and ion-exchange reactions between sediment-bound K^+/Mg^{2+} and pore water NH_4^+ (Santiago Ramos et al., 2018), compensating for any uptake of pore water K and Mg by reverse weathering. In particular, sharp increases in pore water $\delta^{30}Si_{DSi}$ from core-top water values (Fig. 3a and d) suggest that the reverse weathering might take place very soon after sediment deposition (Geilert et al., 2020a; Closset et al., 2022).

4.2.2. Redox conditions and Fe cycling in shallow sediments

Given that the Greenland Ice Sheet (GrIS) acts as an important source of highly reactive iron phases to coastal regions (Hawkings et al., 2014), meltwater from our study sites AM10a and GF-inlet is likely going to be characterized by high concentrations of dissolved Fe and reactive solid Fe phases (Hawkings et al., 2014; Aciego et al., 2015; Hawkings et al., 2018a; Shoenfelt et al., 2019; Pryer et al., 2020; Laufer-Meiser et al., 2021). The fjord system in our study is similar to the BMFC in Chilian Patagonia, characterized by Fe-rich sediments and high pore water Fe concentrations (Ng et al., 2022). Our pore water DSi $\delta^{30}Si$ values observed on the southwest Greenland margin (AM10a and GF-inlet) show similar variation to this analogous location. At this location the heavier pore water Si isotopic composition is associated with Si adsorption to Fe oxy-hydroxides and co-precipitation of amorphous Fe—Si minerals (Ng et al., 2022) under the oxidizing conditions, with the Si isotopic fractionation factor up to −1.6 ‰ (−0.8 ‰ in $^{29}\Delta Si$, Delstanche et al. (2009)) and −3.2 ‰ (Zheng et al., 2016), respectively. Given that the ^{28}Si being preferentially taken up adsorbed and solid phases (Delstanche et al., 2009; Opfergelt et al., 2009; Percak-Dennett et al., 2011; Oelze et al., 2014), the remaining pore water DSi thus presents high $\delta^{30}Si$ values. As the glacially-sourced particles could provide an ample supply of reactive surfaces for Si adsorption within fjordic sediments (van Genuchten et al., 2021; Ng et al., 2022), we hypothesize that the proposed Fe—Si shuttle is also present and has an impact on Si mobility at our study sites.

In addition to the interaction between Si and Fe in the oxic environment near the sediment-water interface, the surfaces of Si-Alk often become covered by Fe oxy-hydroxide coatings, which rapidly reduces Si-Alk dissolution (Michalopoulos and Aller, 2004; Aller, 2014; Wang et al.,

2015). With increasing depth, the oxygen is depleted and sediment enters reducing (nitrogenous, manganous, and ferruginous) conditions. These ferruginous zones are found below 8 cm at AM10a and below 16 cm at GF-inlet, evident by the drastic increase in pore water Fe concentrations (Fig. 3g). In the ferruginous zone, Fe oxy-hydroxides would undergo reductive dissolution, releasing soluble Fe(II) and the previously-bound isotopically light Si (Fig. 5a), as well as removing Si-Alk surface coatings. These reactions thus result in an increase in the solubility of the previously Fe-coated Si-Alk phases and promote DSi release into surrounding pore waters (Mackin, 1989; Delstanche et al., 2009; März et al., 2015; Burdige and Komada, 2020), which is consistent with the positive correlation between Fe and DSi concentration (Fig. 7). Our findings indicate that Si adsorption and desorption via Fe redox cycling is thus likely, acting as another factor influencing the availability of the dynamic DSi pool within pore waters.

Due to the relatively light Si isotopic composition in both Fe(III)-Si coprecipitates and Si-Alk, if Fe oxy-hydroxide reduction dominates early diagenesis, the increasing Fe(II) concentration should lead to a decrease in pore water $\delta^{30}Si_{DSi}$ values. However, there is no correlation between Fe concentration and $\delta^{30}Si_{DSi-pw}$, indicating that other processes (e.g., reverse weathering discussed in Section 4.2.1), which result in a build-up of heavy Si isotopes, are active concurrently with the increasing concentrations of dissolved Fe and DSi within pore waters.

Our pore water data suggests the presence of multiple diagenetic processes: Si-Alk dissolution, reverse weathering and Si—Fe binding that have a competing effect in pore water DSi concentrations, pore water DSi isotopic compositions, and mobility of Si in sediments. Such competing diagenetic processes have previously been identified and evaluated in detail at other high-latitude sites (Cassarino et al., 2020; Closset et al., 2022; Ng et al., 2022; Ward et al., 2022a; Ward et al., 2022b).

4.3. Mechanisms of Si release from fjordic sediments

Our previous discussion focused on the transfer of Si between different phases through Si-Alk dissolution, reverse weathering and cycling associated with Fe redox reactions in fjord sediments. Here, we address the implications of these phase transformations between the different silica pools within the fjord sediments, and quantitatively estimate the contribution of different sources and processes to the overall benthic DSi flux.

Molecular diffusion DSi flux, $J_{diffusion}$, calculated from pore water DSi
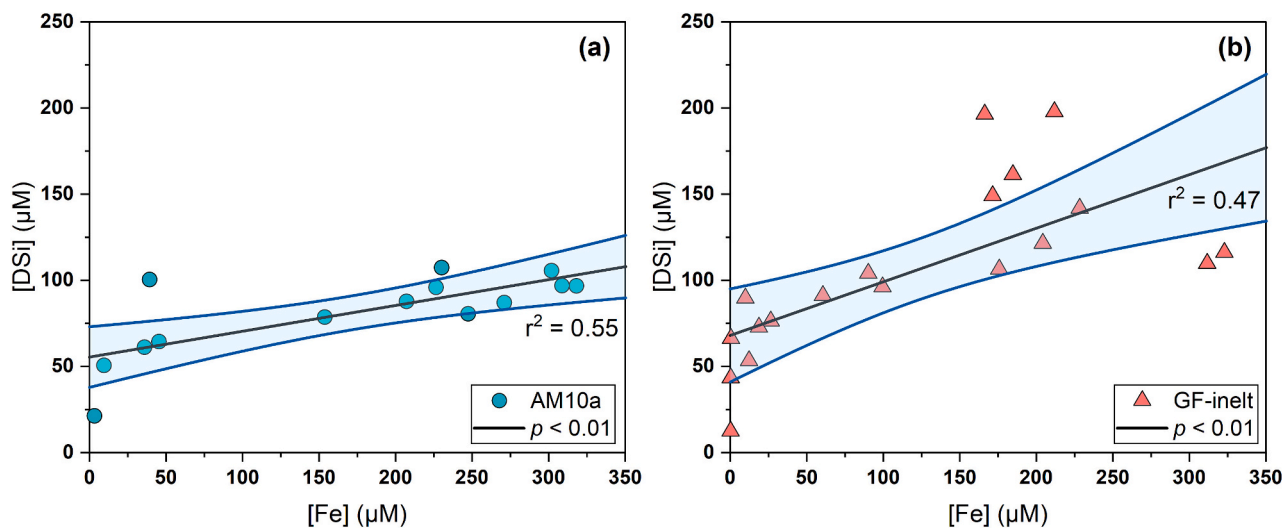
Fig. 7. Linear regression of pore water DSi concentration ([DSi]) against pore water dissolved Fe concentration ([Fe]) at (a) AM10a and (b) GF-inlet. Black lines demonstrate the best fit linear regression and blue lines represent the 95 % confidence interval. The corresponding *p* value and r-square value of each regression line are shown on plot. (For interpretation of the references to colour in this figure legend, the reader is referred to the web version of this article.)

profiles (Table 5), is much smaller than total benthic DSi flux, J_{total}, which is directly measured from the core incubation experiment (Fig. 8). The apparent disparity between total flux and diffusion flux is 0.052 mmol·m^{-2}·day^{-1} at GF-inlet, which is about 3 times larger than $J_{diffusion}$, revealing other DSi contributors except for molecular diffusion. Here, we define this difference as the residual benthic DSi flux, $J_{residual}$ (Table 5), i.e. the flux which is not contributed to by molecular diffusion. The $J_{residual}$ value is estimated using a mass balance calculation:

$$J_{total} = J_{diffusion} + J_{residual} \qquad (7)$$

Assuming that there is no Si isotope fractionation during ASi dissolution (Wetzel et al., 2014) and DSi diffusion (Richter et al., 2006; Oelze et al., 2015), an isotopic mass balance can also be developed for the GF-inlet site (Ng et al., 2020):

$$\frac{d(C \bullet \delta^{30}Si_{core\ incubation})}{d(t/h)} = J_{diffusion} \bullet \delta^{30}Si_{diffusion} + J_{residual} \bullet \delta^{30}Si_{residual} \qquad (8)$$

where $\frac{d(C \bullet \delta^{30}Si_{core\ incubation})}{d(t/h)}$ (Table 5, Fig. S4b in the SI) is the slope of the linear regression between the product of core incubation DSi concentration and its isotopic composition and parameter t/h. We use the $\delta^{30}Si$ of shallow pore water as an approximate representation for $\delta^{30}Si_{diffusion}$ (Table 5). From Eq. (8), $\delta^{30}Si_{residual}$ could be estimated to express the isotope signature of the endmembers responsible for $J_{residual}$ (Table 5).

According to the simple mixing model between shallow pore water and core-top water (Cassarino et al. (2020) and references therein), the intermediate reservoirs, represented by the interface data, fall below the mixing lines at both AM10a and GF-inlet, indicating an additional source of low $\delta^{30}Si$ at the sediment-water interface, such as the dissolution of water column SPM ASi deposited on the core-top water suspended sediments (Fig. 6). Thus, this kind of dissolution plays a key role in providing DSi to core-top water during core incubations, making it a likely contributing factor to $J_{residual}$. Meanwhile, the calculated $\delta^{30}Si_{residual}$ value, +1.53 ‰, is much higher than core-top water $\delta^{30}Si_{ASi-SPM}$, −0.05 ‰ at GF-inlet (Table 5). Therefore, there should be other processes that provide ^{30}Si-rich pore water DSi to the overlying core-top water. Sediment bioirrigation is one possible contributor to $J_{residual}$ and $\delta^{30}Si_{residual}$, as burrowing macrofauna could flush ^{30}Si-enriched pore water DSi to the overlying bottom water (Ng et al., 2020). In addition, any resuspension of the sediment surface (although such resuspension was not observed over the course of incubation experiment) may also introduce an estimation bias or experimental error in J_{total}, and therefore in $J_{residual}$.

Based on the interpretations above, we hypothesize that residual DSi flux derived from our data mainly consists of SPM ASi dissolution, $J_{dissolution}$, and other processes including pore water advection, bioirrigation, and potentially sediment resuspension, J_{other}. In this case, the previous mass balance could be revised with the addition of $J_{dissolution}$ and J_{other}. The former equations could be expanded to the following:

$$J_{total} = J_{diffusion} + J_{dissolution} + J_{other} \qquad (9)$$

$$\frac{d(C \bullet \delta^{30}Si_{core\ incubation})}{d(t/h)} = J_{diffusion} \bullet \delta^{30}Si_{diffusion} + J_{dissolution}$$
$$\bullet \delta^{30}Si_{dissolution} + J_{other} \bullet \delta^{30}Si_{other} \qquad (10)$$

Here, we use $J_{dissolution}$ to describe the benthic DSi flux related to core-top water ASi_{SPM} dissolution and J_{other} to represent the flux
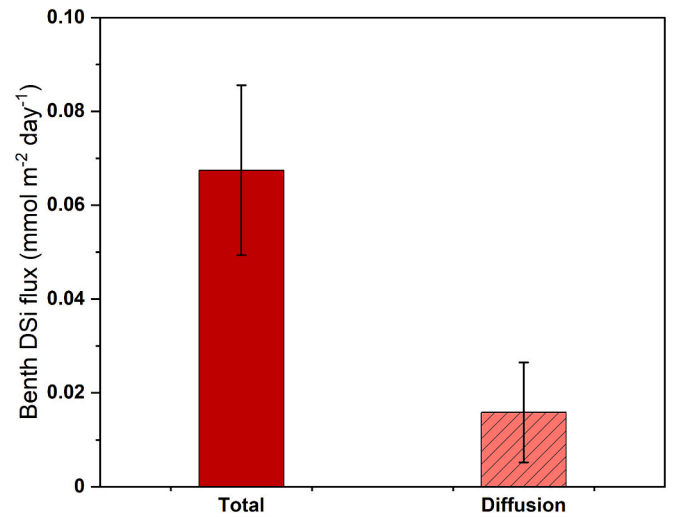
Fig. 8. Benthic DSi fluxes at GF-inlet. The solid column height represents the total benthic DSi fluxes, J_{total}, calculated from the core incubation experiments; while the light-coloured column with dashes indicates diffusion DSi fluxes, $J_{diffusion}$, estimated from pore water DSi profiles using Fick's first law. The uncertainties of J_{total} and $J_{diffusion}$ are represented by black error bars.

associated with previously discussed other pore water DSi release processes (Table 6). The isotopic composition of water column ASi_{SPM} is used as an approximate representation of $\delta^{30}Si_{dissolution}$ (Table 6). Eqs. (9) and (10) help to estimate $J_{dissolution}$ and J_{other}, two main components of $J_{residual}$.

At GF-inlet, the dissolution of water column SPM ASi and other pore water DSi releasing processes contribute to 19 % and 58 % of total benthic DSi flux, respectively. These results imply that glacial marine sediments at or close to fjord heads are subject to non-diffusive processes that can elevate efflux of DSi to the overlying fjord waters.

4.4. Transport of reactive Si from the glacial environment to the coastal regions

4.4.1. Establishing a benthic Si mass balance

In order to further examine the role that fjordic sediments play in the transport of reactive Si from glaciers to offshore environments, we established a benthic mass balance model for the GF-inlet site. Upon sediment deposition, ASi would either be remineralized to DSi and then recycled to the overlying water column, or subsequently buried in deep sediments (Tréguer et al., 2021). The benthic recycling DSi flux has been estimated in the previous section, and so to reconstruct the Si mass balance at the sediment-water interface, the burial flux of ASi is estimated using the following equation (Ragueneau et al., 2009; Hou et al., 2019):

$$J_{burial} = (1 - \phi) \bullet \omega \bullet \rho \bullet ASi_{av} \qquad (11)$$

where ϕ is the porosity of sediment, ω is the sedimentation rate, ρ is the dry density of solid particles, and ASi_{av} refers to the mean value of Si-Alk content deeper than 12 cm where the Si-Alk dissolution rate is not as rapid as the upper sediments, that is, below the depth of the sharply increasing pore water DSi concentration.

Table 5
Benthic DSi flux mass balance parameters.

Site	$\frac{d(C \bullet \delta^{30}Si_{core\ incubation})}{d(t/h)}$	J_{total}	$J_{diffusion}$	$J_{residual}$	$\delta^{30}Si_{diffusion}$	$\delta^{30}Si_{residual}$
	mmol·m^{-2}·day^{-1}	mmol·m^{-2}·day^{-1}	mmol·m^{-2}·day^{-1}	mmol·m^{-2}·day^{-1}	‰	‰
GF-inlet	0.106 ± 0.089	0.067 ± 0.018	0.016 ± 0.011	0.052 ± 0.029	1.70 ± 0.07	1.53 ± 1.24

Table 6
Benthic DSi flux mass balance parameters.

Site	$\dfrac{d(C \cdot \delta^{30}Si_{core\ incubation})}{d(t/h)}$	J_{total}	$J_{diffusion}$		$J_{dissolution}$		J_{other}		$\delta^{30}Si_{diffusion}$	$\delta^{30}Si_{dissolution}$	$\delta^{30}Si_{other}$
	mmol·m⁻²·day⁻¹	mmol·m⁻²·day⁻¹	mmol·m⁻²·day⁻¹	% J_{total}	mmol·m⁻²·day⁻¹	% J_{total}	mmol·m⁻²·day⁻¹	% J_{total}	‰	‰	‰
GF-inlet	0.106	0.067	0.016	23	0.028	19	0.024	58	1.70	−0.05	2.05

The rain rate of ASi that reaches the bottom of the fjord is defined as the sum of burial flux, J_{burial}, and the fraction of ASi that is recycled into silicic acid, J_{total}, assuming that all ASi would either dissolve or be preserved:

$$ASi\ rain = J_{total} + J_{burial} \tag{12}$$

$$Burial\ efficiency = \frac{J_{burial}}{ASi\ rain} \times 100\% \tag{13}$$

With these estimated values (Table 7), the benthic Si mass balance between Nuup Kangerlua and its adjacent Southwest Greenland continental shelf can be developed (Fig. 9a).

The estimated (total) benthic DSi flux at GF-inlet: 25 mmol m^{-2} yr^{-1} is substantially lower than values found at the Southwest Greenland margin: 164–1121 mmol m^{-2} yr^{-1}) (Ng et al., 2020) (Fig. 9a, Table 7). The low benthic DSi flux at GF-inlet is likely due to the high burial efficiency of dissolvable ASi: 98 %, relative to the adjacent continental margin sites: 11–72 % (Table 7). Such high burial efficiency of ASi (~99 %) has also been previously observed at the other fjord study in Chilean Patagonia (Ng et al., 2022).

4.4.2. Glacially-derived reactive Si phase transport in fjords

Extrapolating data obtained from the GF-inlet site to the entire fjord area (Fig. 9b, Table 8) may pose some uncertainties, as benthic DSi flux is expected to increase with a general decrease in sedimentation rate further down a fjord (Ng et al., 2022). Despite these uncertainties, extrapolating the new data could still provide useful insights that improve our understanding of the cycling and transport of nutrient Si across a fjord. Compared with nonglacial rivers at the lower latitudes (Tréguer et al., 2021), export of reactive Si from GrIS is mainly through glaciers and in the form of reactive particulate ASi (Fig. 9b, Table 8), and our evaluation suggests that up to half of the glacial ASi is buried in the fjordic sediments (Fig. 9b). The high burial flux of dissolvable ASi and the low benthic DSi return flux inferred here (Fig. 9b) makes fjordic sediments a potentially large sink/trap for glacier-sourced reactive Si phases.

The estimated benthic DSi flux in Nuup Kangerlua: ~50 × 10^6 mol yr^{-1} and the glacial DSi input to the fjord: ~100 × 10^6 mol yr^{-1} are both small and unlikely to account for the total diatom BSi production in the fjord: ~2440 × 10^6 mol yr^{-1} (Fig. 9b, Table 8). Meanwhile, despite rapid burial in fjordic sediments, the remaining portion of glacial ASi that is either suspended in the water column, or dissolving in the fjord water, is estimated to be a large reservoir: ~2560 × 10^6 mol yr^{-1}. We suggest that this large pool of dissolving glacial ASi in the water column acts as the most important conduit of biologically available Si from glaciers to the offshore environment, sustaining diatom primary production in the fjords and potentially also in the coastal environment. In addition to the offshore transport of dissolving glacial ASi, remineralization of dead diatoms, active benthic-pelagic coupling and upwelling processes, all likely contribute to the relatively high diatom primary production observed off the coast of southwest Greenland (Fig. 9a) (Hendry et al., 2019; Ng et al., 2020).

5. Conclusions

This study presents incubation experiments and analyses of sediment and pore water profiles, including silicon isotope analysis, to evaluate benthic DSi fluxes within SW Greenlandic fjords. Si isotopic compositions of pore water, sediment ASi, glacially-derived ASi, and overlying bottom waters demonstrate competing early diagenetic processes that influence the build-up of pore water silicic acid. These competing processes mainly include: the dissolution of soluble ASi, precipitation reactions like reverse weathering, and association with Fe redox cycling in fjord sediments. These early diagenetic processes result in a concentration gradient at the sediment-water interface which regulates the molecular diffusive transport of DSi from pore water to the overlying water

Table 7

Benthic flux of reactive Si phases calculated for Nuup Kangerlua and the adjacent coast, and the parameters involved in the calculation.

Site	Region	Latitude	Longitude	J_{total}	φ	ω	ρ	ASi_{av}	J_{burial}	ASi rain	Burial efficiency	Reference
		°N	°E	mmol m^{-2} yr^{-1}		cm yr^{-1}	g cm^{-3}	µmol/ g	mmol m^{-2} yr^{-1}	mmol m^{-2} yr^{-1}	%	
GF-inlet	Nuup Kangerlua	64.7594	−50.6271	24.62	0.61	1.1 ± 0.6	2.3	143.3	1391.05	1415.67	98	This study
MGA3	South West Greenland margin (off Nuuk)	63.8154	−53.7743	678.90	0.51	0.11 ± 0.03	2.5	145.16	194.01	872.91	22	(Ng et al., 2020)
MGA4		63.5530	−52.2251	164.25	0.71	0.16 ± 0.02	2.5	375.11	430.62	594.87	72	(Ng et al., 2020)
MGA5	South Greenland margin (off Narsaq)	60.2618	−46.8908	1120.55	0.40	0.06 ± 0.01	2.5	154.73	140.42	1260.97	11	(Ng et al., 2020)
MGA6		60.1160	−46.6635	189.80	0.66	0.06 ± 0.01	2.5	122.22	63.06	252.86	25	(Ng et al., 2020)
MGA7	South Greenland margin (off Cape Farewell)	59.4564	−44.4151	222.65	0.42	0.06 ± 0.01	2.5	134.54	117.25	339.90	34	(Ng et al., 2020)

Definition: J_{total} – total benthic DSi flux calculated from core incubation experiments; φ – the porosity of sediment; ω – sedimentation rate estimated based on ^{210}Pb measurements (Ng et al., 2020; Oksman et al., 2022), and for site GF-inlet, data are taken from a nearby fjord station (Oksman et al., 2022); ρ – the dry density of solid particles; ASi_{av} – the average of the Si-Alk content below 12 cm; J_{burial} – burial flux of ASi; ASi rain – the sum of J_{total} and J_{burial}; Burial efficiency – the ratio of J_{bruail} over ASi rain.
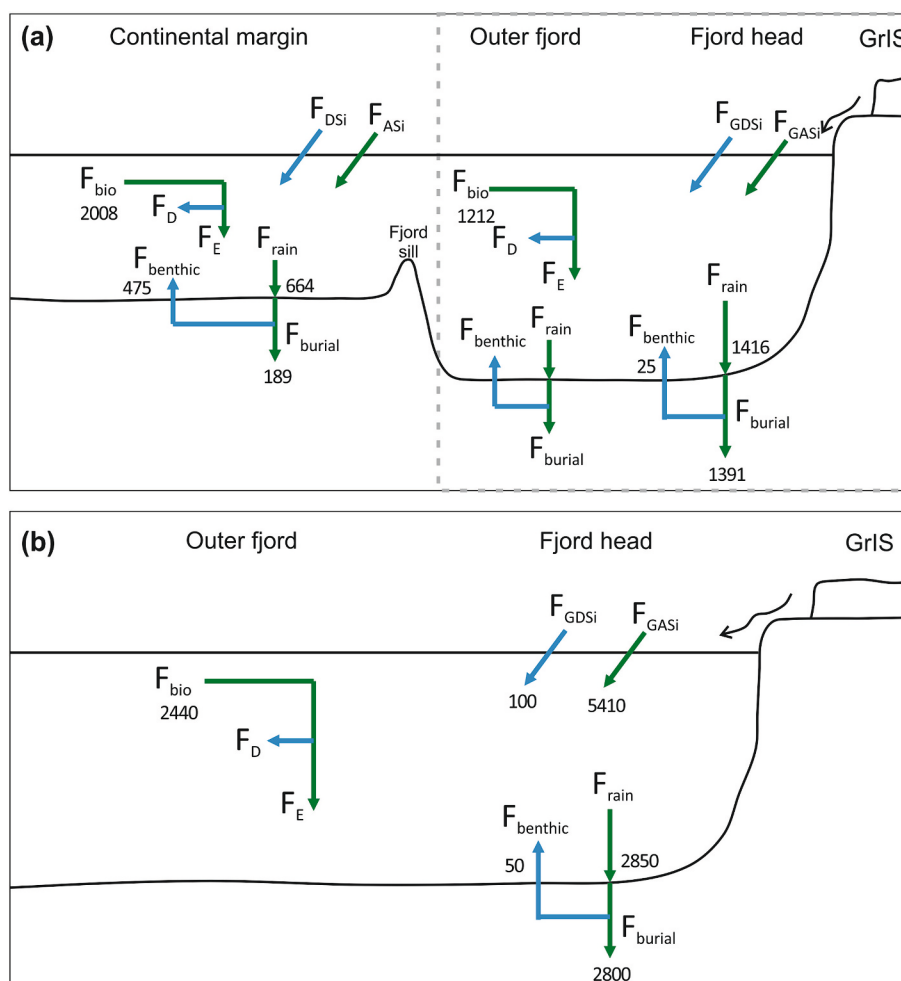
Fig. 9. (a) Schematic view of the Si cycle in the glacial marine environment at Southwest Greenland, with area-normalised flux (F) in mmol m^{-2} yr^{-1}. (b) Schematic view of the Si cycle in Nuup Kangerlua fjord, with total flux in 10^6 mol yr^{-1}. Green arrows correspond to ASi flux, including glacial ASi input (F$_{GASi}$), continental ASi input (F$_{ASi}$), ASi rain (F$_{rain}$), burial flux (F$_{burial}$), BSi production (F$_{bio}$), and BSi export (F$_E$). F$_{bio}$ is estimated through previously confirmed primary production from Hendry et al. (2019) (continental margin) and Meire et al. (2017) (outer fjord). Blue arrows indicate DSi flux, including glacial DSi input (F$_{GDSi}$), continental DSi input (F$_{DSi}$), BSi dissolution (F$_D$), and benthic DSi flux (F$_{benthic}$). Estimation has not been carried out for F$_D$, F$_E$, F$_{DSi}$, F$_{ASi}$, and benthic Si cycling at the outer fjord, given the lack of such data in existing literature. (For interpretation of the references to colour in this figure legend, the reader is referred to the web version of this article.)

Table 8
Mean Si concentrations and estimated flux for Nuup Kangerlua.

Location	Input	Discharge	Area	DSi	ASi	DSi input	ASi input	J_{total}	J_{burial}	ASi rain
		km^3 yr^{-1}	km^2	µmol dm^{-3}	µmol dm^{-3}	10^6 mol yr^{-1}	10^6 mol yr^{-1}	10^6 mol yr^{-1}	10^6 mol yr^{-1}	10^6 mol yr^{-1}
Nuup Kangerlua	Marine-terminating glaciers	18.4	2013	3.85 (0.18–14.33)	208.85 (9.66–2017.78)	70.90	3842.91	49.56	2800.19	2849.75
	Land-terminating glaciers	7.5				28.90	1566.40			
	Total freshwater	25.9				99.80	5409.31			

Note: Fjord area and discharge data are taken from Stuart-Lee et al. (2021). The concentration of ASi is an average of suspended ASi concentrations in the water column at Nuup Kangerlua (Hatton et al., 2023).

column, also known as the diffusive benthic DSi flux. The significant difference between the diffusive DSi flux and total benthic DSi flux from core incubations indicates that other mechanisms contribute to sediment efflux of DSi. Our isotope mass balance model suggests that processes contributing to benthic DSi flux include molecular diffusion, rapid glacial ASi dissolution, and other processes including advective pore water mixing, sediment bioirrigation, and potential surface resuspension. Benthic DSi flux evaluated at the inner fjord is much smaller than the surrounding Greenland margin sites. The limited return flux of DSi from sediments into the overlying fjord water column and the high burial flux of ASi makes fjord (head) sediments an efficient trap for glacier-sourced reactive Si phases. Despite the high burial flux of ASi, the remaining dissolving glacial ASi still has a large reservoir, and could act as an important conduit of biologically available Si from glaciers to fjords and also further offshore, contributing to sustaining primary production in the downstream marine environment.

CRediT authorship contribution statement

Tong Wang: Writing – review & editing, Writing – original draft, Validation, Methodology, Investigation, Formal analysis, Conceptualization. **Hong Chin Ng:** Writing – review & editing, Writing – original draft, Validation, Methodology, Investigation, Formal analysis, Conceptualization. **Jade E. Hatton:** Writing – review & editing, Writing – original draft, Methodology. **Samantha J. Hammond:** Writing – review & editing, Writing – original draft, Validation, Methodology, Investigation. **E. Malcolm S. Woodward:** Writing – review & editing, Writing – original draft, Validation, Methodology, Investigation. **Lorenz Meire:** Writing – review & editing, Writing – original draft. **Katharine R. Hendry:** Writing – review & editing, Writing – original draft, Supervision, Resources, Methodology, Formal analysis, Conceptualization.

Declaration of competing interest

The authors declare that they have no known competing financial interests or personal relationships that could have appeared to influence the work reported in this paper.

Data availability

Research data associated with this article are available at PANGAEA Data Publisher (Wang et al., 2023) via https://doi.org/10.1594/PANGAEA.961726.

Acknowledgments

Appendix A. Supplementary data

Supplementary data to this article can be found online at https://doi.org/10.1016/j.chemgeo.2024.122403.

References

Aciego, S.M., Stevenson, E.I., Arendt, C.A., 2015. Climate versus geological controls on glacial meltwater micronutrient production in southern Greenland. Earth Planet. Sci. Lett. 424, 51–58. https://doi.org/10.1016/j.epsl.2015.05.017.

Aller, R.C., 2014. Sedimentary diagenesis, depositional environments, and benthic fluxes. Treatise Geochem. 293–334.

Andrews, E., Pogge von Strandmann, P.A.E., Fantle, M.S., 2020. Exploring the importance of authigenic clay formation in the global Li cycle. Geochim. Cosmochim. Acta 289, 47–68. https://doi.org/10.1016/j.gca.2020.08.018.

Baronas, J.J., Hammond, D.E., Berelson, W.M., McManus, J., Severmann, S., 2016. Germanium–silicon fractionation in a river-influenced continental margin: the Northern Gulf of Mexico. Geochim. Cosmochim. Acta 178, 124–142. https://doi.org/10.1016/j.gca.2016.01.028.

Becker, S., Aoyama, M., Woodward, E.M.S., Bakker, K., Coverly, S., Mahaffey, C., Tanhua, T., 2020. GO-SHIP repeat Hydrography Nutrient Manual: the precise and accurate determination of dissolved inorganic nutrients in seawater, using continuous flow analysis methods. Front. Mar. Sci. 7 https://doi.org/10.3389/fmars.2020.581790.

Bianchi, T.S., Arndt, S., Austin, W.E.N., Benn, D.I., Bertrand, S., Cui, X., Syvitski, J., 2020. Fjords as aquatic critical zones (ACZs). Earth Sci. Rev. 203 https://doi.org/10.1016/j.earscirev.2020.103145.

Boudreau, B.P., 1996. The diffusive tortuosity of fine-grained unlithified sediments. Geochim. Cosmochim. Acta 60 (16), 3139–3142. https://doi.org/10.1016/0016-7037(96)00158-5.

Burdige, D.J., Komada, T., 2020. Iron redox cycling, sediment resuspension and the role of sediments in low oxygen environments as sources of iron to the water column. Mar. Chem. 223 https://doi.org/10.1016/j.marchem.2020.103793.

Cardinal, D., Alleman, L.Y., de Jong, J., Ziegler, K., André, L., 2003. Isotopic composition of silicon measured by multicollector plasma source mass spectrometry in dry plasma mode. J. Anal. At. Spectrom. 18 (3), 213–218. https://doi.org/10.1039/b210109b.

Cassarino, L., Hendry, K.R., Henley, S.F., MacDonald, E., Arndt, S., Freitas, F.S., Firing, Y.L., 2020. Sedimentary nutrient supply in productive hot spots off the west antarctic peninsula revealed by silicon isotopes. Glob. Biogeochem. Cycles 34 (12). https://doi.org/10.1029/2019gb006486.

Closset, I., Brzezinski, M.A., Cardinal, D., Dapoigny, A., Jones, J.L., Robinson, R.S., 2022. A silicon isotopic perspective on the contribution of diagenesis to the sedimentary silicon budget in the Southern Ocean. Geochim. Cosmochim. Acta 327, 298–313. https://doi.org/10.1016/j.gca.2022.04.010.

de Laeter, J.R., Böhlke, J.K., De Bièvre, P., Hidaka, H., Peiser, H.S., Rosman, K.J.R., Taylor, P.D.P., 2003. Atomic weights of the elements. Review 2000 (IUPAC Technical Report). Pure Appl. Chem. 75 (6), 683–800. https://doi.org/10.1351/pac200375060683.

de Souza, G.F., Reynolds, B.C., Rickli, J., Frank, M., Saito, M.A., Gerringa, L.J.A., Bourdon, B., 2012. Southern ocean control of silicon stable isotope distribution in the deep Atlantic Ocean. Glob. Biogeochem. Cycles 26 (2). https://doi.org/10.1029/2011gb004141.

Delstanche, S., Opfergelt, S., Cardinal, D., Elsass, F., André, L., Delvaux, B., 2009. Silicon isotopic fractionation during adsorption of aqueous monosilicic acid onto iron oxide. Geochim. Cosmochim. Acta 73 (4), 923–934. https://doi.org/10.1016/j.gca.2008.11.014.

DeMaster, D.J., 1981. The supply and accumulation of silica in the marine environment. Geochim. Cosmochim. Acta 45 (10), 1715–1732. https://doi.org/10.1016/0016-7037(81)90006-5.

Dixit, S., Van Cappellen, P., van Bennekom, A.J., 2001. Processes controlling solubility of biogenic silica and pore water build-up of silicic acid in marine sediments. Mar. Chem. 73 (3), 333–352. https://doi.org/10.1016/S0304-4203(00)00118-3.

Ehlert, C., Grasse, P., Mollier-Vogel, E., Böschen, T., Franz, J., de Souza, G.F., Frank, M., 2012. Factors controlling the silicon isotope distribution in waters and surface sediments of the Peruvian coastal upwelling. Geochim. Cosmochim. Acta 99, 128–145. https://doi.org/10.1016/j.gca.2012.09.038.

Ehlert, C., Doering, K., Wallmann, K., Scholz, F., Sommer, S., Grasse, P., Frank, M., 2016. Stable silicon isotope signatures of marine pore waters – Biogenic opal dissolution versus authigenic clay mineral formation. Geochim. Cosmochim. Acta 191, 102–117. https://doi.org/10.1016/j.gca.2016.07.022.

Frings, P., 2017. Revisiting the dissolution of biogenic Si in marine sediments: a key term in the ocean Si budget. Acta Geochimica 36 (3), 429–432. https://doi.org/10.1007/s11631-017-0183-1.

Frings, P.J., Clymans, W., Fontorbe, G., De La Rocha, C.L., Conley, D.J., 2016. The continental Si cycle and its impact on the ocean Si isotope budget. Chem. Geol. 425, 12–36. https://doi.org/10.1016/j.chemgeo.2016.01.020.

Geilert, S., Vroon, P.Z., van Bergen, M.J., 2016. Effect of diagenetic phase transformation on the silicon isotope composition of opaline sinter deposits of Geysir, Iceland. Chem. Geol. 433, 57–67. https://doi.org/10.1016/j.chemgeo.2016.04.008.

Geilert, S., Grasse, P., Doering, K., Wallmann, K., Ehlert, C., Scholz, F., Hensen, C., 2020a. Impact of ambient conditions on the Si isotope fractionation in marine pore fluids during early diagenesis. Biogeosciences 17 (7), 1745–1763. https://doi.org/10.5194/bg-17-1745-2020.

Geilert, S., Grasse, P., Wallmann, K., Liebetrau, V., Menzies, C.D., 2020b. Serpentine alteration as source of high dissolved silicon and elevated delta(30)Si values to the marine Si cycle. Nat. Commun. 11 (1), 5123. https://doi.org/10.1038/s41467-020-18804-y.

Georg, R.B., Reynolds, B.C., Frank, M., Halliday, A.N., 2006. New sample preparation techniques for the determination of Si isotopic compositions using MC-ICPMS. Chem. Geol. 235 (1–2), 95–104. https://doi.org/10.1016/j.chemgeo.2006.06.006.

Grasse, P., Brzezinski, M.A., Cardinal, D., de Souza, G.F., Andersson, P., Closset, I., Zhang, Z., 2017. GEOTRACES inter-calibration of the stable silicon isotope composition of dissolved silicic acid in seawater. J. Anal. At. Spectrom. 32 (3), 562–578. https://doi.org/10.1039/c6ja00302h.

Hammond, D.E., Cummins, K.M., McManus, J., Berelson, W.M., Smith, G., Spagnoli, F., 2004. Methods for measuring benthic nutrient flux on the California margin: comparing shipboard core incubations to in situ lander results. Limnol. Oceanogr. Methods 2 (6), 146–159. https://doi.org/10.4319/lom.2004.2.146.

Hatton, J.E., Hendry, K.R., Hawkings, J.R., Wadham, J.L., Kohler, T.J., Stibal, M., Telling, J., 2019. Investigation of subglacial weathering under the Greenland Ice Sheet using silicon isotopes. Geochim. Cosmochim. Acta 247, 191–206. https://doi.org/10.1016/j.gca.2018.12.033.

Hatton, J.E., Ng, H.C., Meire, L., Woodward, E.M.S., Leng, M.J., Coath, C.D., Hendry, K.R., 2023. Silicon isotopes highlight the role of glaciated fjords in modifying coastal waters. J. Geophys. Res. Biogeosci. 128 (7) https://doi.org/10.1029/2022jg007242.

Hawkings, J.R., Wadham, J.L., Tranter, M., Raiswell, R., Benning, L.G., Statham, P.J., Telling, J., 2014. Ice sheets as a significant source of highly reactive nanoparticulate iron to the oceans. Nat. Commun. 5, 3929. https://doi.org/10.1038/ncomms4929.

Hawkings, J.R., Wadham, J.L., Benning, L.G., Hendry, K.R., Tranter, M., Tedstone, A., Raiswell, R., 2017. Ice sheets as a missing source of silica to the polar oceans. Nat. Commun. 8, 14198. https://doi.org/10.1038/ncomms14198.

Hawkings, J.R., Benning, L.G., Raiswell, R., Kaulich, B., Araki, T., Abyaneh, M., Tranter, M., 2018a. Biolabile ferrous iron bearing nanoparticles in glacial sediments. Earth Planet. Sci. Lett. 493, 92–101. https://doi.org/10.1016/j.epsl.2018.04.022.

Hawkings, J.R., Hatton, J.E., Hendry, K.R., de Souza, G.F., Wadham, J.L., Ivanovic, R., Tranter, M., 2018b. The silicon cycle impacted by past ice sheets. Nat. Commun. 9 (1), 3210. https://doi.org/10.1038/s41467-018-05689-1.

Hendry, K.R., Robinson, L.F., 2012. The relationship between silicon isotope fractionation in sponges and silicic acid concentration: Modern and core-top studies of biogenic opal. Geochim. Cosmochim. Acta 81, 1–12. https://doi.org/10.1016/j.gca.2011.12.010.

Hendry, K.R., Huvenne, V.A.I., Robinson, L.F., Annett, A., Badger, M., Jacobel, A.W., Woodward, E.M.S., 2019. The biogeochemical impact of glacial meltwater from Southwest Greenland. Prog. Oceanogr. 176 https://doi.org/10.1016/j.pocean.2019.102126.

Hoffmann, J.E., Svahnberg, H., Piazolo, S., Scherstén, A., Münker, C., 2012. The geodynamic evolution of Mesoarchean anorthosite complexes inferred from the Naajat Kuuat complex, southern West Greenland. Precambrian Res. 196-197, 149–170. https://doi.org/10.1016/j.precamres.2011.12.002.

Hopwood, M.J., Carroll, D., Dunse, T., Hodson, A., Holding, J.M., Iriarte, J.L., Meire, L., 2020. Review article: how does glacier discharge affect marine biogeochemistry and primary production in the Arctic? Cryosphere 14 (4), 1347–1383. https://doi.org/10.5194/tc-14-1347-2020.

Hou, Y., Hammond, D.E., Berelson, W.M., Kemnitz, N., Adkins, J.F., Lunstrum, A., 2019. Spatial patterns of benthic silica flux in the North Pacific reflect upper ocean production. Deep-Sea Res. I Oceanogr. Res. Pap. 148, 25–33. https://doi.org/10.1016/j.dsr.2019.04.013.

Huettel, M., Ziebis, W., Forster, S., Luther, G.W., 1998. Advective transport affecting metal and nutrient distributions and interfacial fluxes in permeable sediments. Geochim. Cosmochim. Acta 62 (4), 613–631. https://doi.org/10.1016/s0016-7037(97)00371-2.

Hughes, H.J., Delvigne, C., Korntheuer, M., de Jong, J., André, L., Cardinal, D., 2011. Controlling the mass bias introduced by anionic and organic matrices in silicon isotopic measurements by MC-ICP-MS. J. Anal. At. Spectrom. 26 (9) https://doi.org/10.1039/c1ja10110b.

Hughes, H.J., Sondag, F., Santos, R.V., André, L., Cardinal, D., 2013. The riverine silicon isotope composition of the Amazon Basin. Geochim. Cosmochim. Acta 121, 637–651. https://doi.org/10.1016/j.gca.2013.07.040.

Janssen, F., Huettel, M., Witte, U., 2005. Pore-water advection and solute fluxes in permeable marine sediments (II): Benthic respiration at three sandy sites with different permeabilities (German Bight, North Sea). Limnol. Oceanogr. 50 (3), 779–792. https://doi.org/10.4319/lo.2005.50.3.0779.

Jiang, X., Lin, X., Yao, D., Zhai, S., Guo, W., 2007. Geochemistry of lithium in marine ferromanganese oxide deposits. Deep-Sea Res. I Oceanogr. Res. Pap. 54 (1), 85–98. https://doi.org/10.1016/j.dsr.2006.10.004.

Karl, D.M., Tien, G., 1992. MAGIC: a sensitive and precise method for measuring dissolved phosphorus in aquatic environments. Limnol. Oceanogr. 37 (1), 105–116. https://doi.org/10.4319/lo.1992.37.1.0105.

Krause, J.W., Duarte, C.M., Marquez, I.A., Assmy, P., Fernández-Méndez, M., Wiedmann, I., Agustí, S., 2018. Biogenic silica production and diatom dynamics in the Svalbard region during spring. Biogeosciences 15 (21), 6503–6517. https://doi.org/10.5194/bg-15-6503-2018.

Krause, J.W., Schulz, I.K., Rowe, K.A., Dobbins, W., Winding, M.H.S., Sejr, M.K., Agusti, S., 2019. Silicic acid limitation drives bloom termination and potential carbon sequestration in an Arctic bloom. Sci. Rep. 9 (1), 8149. https://doi.org/10.1038/s41598-019-44587-4.

Krissansen-Totton, J., Catling, D.C., 2020. A coupled carbon-silicon cycle model over Earth history: reverse weathering as a possible explanation of a warm mid-Proterozoic climate. Earth Planet. Sci. Lett. 537 https://doi.org/10.1016/j.epsl.2020.116181.

Lam, P.J., Ohnemus, D.C., Auro, M.E., 2015. Size-fractionated major particle composition and concentrations from the US GEOTRACES North Atlantic Zonal Transect. Deep-Sea Res. II Top. Stud. Oceanogr. 116, 303–320. https://doi.org/10.1016/j.dsr2.2014.11.020.

Laufer-Meiser, K., Michaud, A.B., Maisch, M., Byrne, J.M., Kappler, A., Patterson, M.O., Jorgensen, B.B., 2021. Potentially bioavailable iron produced through benthic cycling in glaciated Arctic fjords of Svalbard. Nat. Commun. 12 (1), 1349. https://doi.org/10.1038/s41467-021-21558-w.

Loucaides, S., Koning, E., Van Cappellen, P., 2012. Effect of pressure on silica solubility of diatom frustules in the oceans: results from long-term laboratory and field incubations. Mar. Chem. 136-137, 1–6. https://doi.org/10.1016/j.marchem.2012.04.003.

Mackenzie, F.T., Garrels, R.M., 1966. Chemical mass balance between rivers and oceans. Am. J. Sci. 264, 507–525.

Mackin, J.E., 1989. Relationships between Si, Al, and Fe deposited on filter-covered glass substrates in marine sediments and in suspensions of sediments and standard clays. Mar. Chem. 26 (2), 101–117. https://doi.org/10.1016/0304-4203(89)90055-8.

Maldonado, M., López-Acosta, M., Sitjà, C., García-Puig, M., Galobart, C., Ercilla, G., Leynaert, A., 2019. Sponge skeletons as an important sink of silicon in the global oceans. Nat. Geosci. 12 (10), 815–822. https://doi.org/10.1038/s41561-019-0430-7.

Martin, J.B., Kastner, M., Elderfield, H., 1991. Lithium: sources in pore fluids of Peru slope sediments and implications for oceanic fluxes. Mar. Geol. 102 (1), 281–292. https://doi.org/10.1016/0025-3227(91)90012-S.

März, C., Meinhardt, A.K., Schnetger, B., Brumsack, H.J., 2015. Silica diagenesis and benthic fluxes in the Arctic Ocean. Mar. Chem. 171, 1–9. https://doi.org/10.1016/j.marchem.2015.02.003.

McManus, J., Hammond, D.E., Berelson, W.M., Kilgore, T.E., Demaster, D.J., Ragueneau, O.G., Collier, R.W., 1995. Early diagenesis of biogenic opal: Dissolution rates, kinetics, and paleoceanographic implications. Deep-Sea Res. II Top. Stud. Oceanogr. 42 (2–3), 871–903. https://doi.org/10.1016/0967-0645(95)00035-o.

Meire, L., Meire, P., Struyf, E., Krawczyk, D.W., Arendt, K.E., Yde, J.C., Meysman, F.J.R., 2016. High export of dissolved silica from the Greenland Ice Sheet. Geophys. Res. Lett. 43 (17), 9173–9182. https://doi.org/10.1002/2016gl070191.

Meire, L., Mortensen, J., Meire, P., Juul-Pedersen, T., Sejr, M.K., Rysgaard, S., Meysman, F.J.R., 2017. Marine-terminating glaciers sustain high productivity in Greenland fjords. Glob. Chang. Biol. 23 (12), 5344–5357. https://doi.org/10.1111/gcb.13801.

Michalopoulos, P., Aller, R.C., 1995. Rapid clay mineral formation in amazon delta sediments: reverse weathering and oceanic elemental cycles. Science 270 (5236), 614–617. https://doi.org/10.1126/science.270.5236.614.

Michalopoulos, P., Aller, R.C., 2004. Early diagenesis of biogenic silica in the Amazon delta: alteration, authigenic clay formation, and storage. Geochim. Cosmochim. Acta 68 (5), 1061–1085. https://doi.org/10.1016/j.gca.2003.07.018.

Mortensen, J., Lennert, K., Bendtsen, J., Rysgaard, S., 2011. Heat sources for glacial melt in a sub-Arctic fjord (Godthåbsfjord) in contact with the Greenland Ice Sheet. J. Geophys. Res. 116 (C1) https://doi.org/10.1029/2010jc006528.

Mortensen, J., Rysgaard, S., Arendt, K.E., Juul-Pedersen, T., Søgaard, D.H., Bendtsen, J., Meire, L., 2018. Local coastal water masses control heat levels in a west greenland tidewater outlet glacier fjord. J. Geophys. Res. Oceans 123 (11), 8068–8083. https://doi.org/10.1029/2018jc014549.

Ng, H.C., Cassarino, L., Pickering, R.A., Woodward, E.M.S., Hammond, S.J., Hendry, K.R., 2020. Sediment efflux of silicon on the Greenland margin and implications for the marine silicon cycle. Earth Planet. Sci. Lett. 529 https://doi.org/10.1016/j.epsl.2019.115877.

Ng, H.C., Hawkings, J.R., Bertrand, S., Summers, B.A., Sieber, M., Conway, T.M., Hendry, K.R., 2022. Benthic dissolved silicon and iron cycling at glaciated

patagonian fjord heads. Glob. Biogeochem. Cycles 36 (11), e2022GB007493. https://doi.org/10.1029/2022GB007493.

Oelze, M., von Blanckenburg, F., Hoellen, D., Dietzel, M., Bouchez, J., 2014. Si stable isotope fractionation during adsorption and the competition between kinetic and equilibrium isotope fractionation: Implications for weathering systems. Chem. Geol. 380, 161–171. https://doi.org/10.1016/j.chemgeo.2014.04.027.

Oelze, M., von Blanckenburg, F., Bouchez, J., Hoellen, D., Dietzel, M., 2015. The effect of Al on Si isotope fractionation investigated by silica precipitation experiments. Chem. Geol. 397, 94–105. https://doi.org/10.1016/j.chemgeo.2015.01.002.

Oksman, M., Kvorning, A.B., Larsen, S.H., Kjeldsen, K.K., Mankoff, K.D., Colgan, W., Ribeiro, S., 2022. Impact of freshwater runoff from the Southwest Greenland Ice Sheet on fjord productivity since the late 19th century. Cryosphere 16 (6), 2471–2491. https://doi.org/10.5194/tc-16-2471-2022.

Opfergelt, S., Delmelle, P., 2012. Silicon isotopes and continental weathering processes: Assessing controls on Si transfer to the ocean. Compt. Rendus Geosci. 344 (11–12), 723–738. https://doi.org/10.1016/j.crte.2012.09.006.

Opfergelt, S., de Bournonville, G., Cardinal, D., André, L., Delstanche, S., Delvaux, B., 2009. Impact of soil weathering degree on silicon isotopic fractionation during adsorption onto iron oxides in basaltic ash soils,Cameroon. Geochimica et Cosmochimica Acta 73 (24), 7226–7240. https://doi.org/10.1016/j.gca.2009.09.003.

Percak-Dennett, E.M., Beard, B.L., Xu, H., Konishi, H., Johnson, C.M., Roden, E.E., 2011. Iron fractionation during microbial dissimilatory iron oxide reduction in simulated Archaean seawater. Geobiology 9 (3), 205–220. https://doi.org/10.1111/j.1472-4669.2011.00277.x.

Pickering, R.A., Cassarino, L., Hendry, K.R., Wang, X.L., Maiti, K., Krause, J.W., 2020. Using stable isotopes to disentangle marine sedimentary signals in reactive silicon pools. Geophys. Res. Lett. 47 (15) https://doi.org/10.1029/2020gl087877.

Polat, A., Longstaffe, F.J., Frei, R., 2018. An overview of anorthosite-bearing layered intrusions in the Archaean craton of southern West Greenland and the Superior Province of Canada: implications for Archaean tectonics and the origin of megacrystic plagioclase. Geodin. Acta 30 (1), 84–99. https://doi.org/10.1080/09853111.2018.1427408.

Pryer, H.V., Hawkings, J.R., Wadham, J.L., Robinson, L.F., Hendry, K.R., Hatton, J.E., Häussermann, V., 2020. The influence of glacial cover on riverine silicon and iron exports in chilean patagonia. Glob. Biogeochem. Cycles 34 (12), e2020GB006611. https://doi.org/10.1029/2020GB006611.

Ragueneau, O., Savoye, N., Del Amo, Y., Cotten, J., Tardiveau, B., Leynaert, A., 2005. A new method for the measurement of biogenic silica in suspended matter of coastal waters: using Si:Al ratios to correct for the mineral interference. Cont. Shelf Res. 25 (5–6), 697–710. https://doi.org/10.1016/j.csr.2004.09.017.

Ragueneau, O., Regaudie-de-Gioux, A., Moriceau, B., Gallinari, M., Vangriesheim, A., Baurand, F., Khripounoff, A., 2009. A benthic Si mass balance on the Congo margin: Origin of the 4000m DSi anomaly and implications for the transfer of Si from land to ocean. Deep-Sea Res. II Top. Stud. Oceanogr. 56 (23), 2197–2207. https://doi.org/10.1016/j.dsr2.2009.04.003.

Rahman, S., 2019. Reverse weathering reactions in marine sediments. Encyclopedia Ocean Sci. 216–227.

Rebreanu, L., Vanderborght, J.-P., Chou, L., 2008. The diffusion coefficient of dissolved silica revisited. Mar. Chem. 112 (3–4), 230–233. https://doi.org/10.1016/j.marchem.2008.08.004.

Reynolds, B., Frank, M., Halliday, A., 2006a. Silicon isotope fractionation during nutrient utilization in the North Pacific. Earth Planet. Sci. Lett. 244 (1–2), 431–443. https://doi.org/10.1016/j.epsl.2006.02.002.

Reynolds, B.C., Georg, R.B., Oberli, F., Wiechert, U., Halliday, A.N., 2006b. Re-assessment of silicon isotope reference materials using high-resolution multi-collector ICP-MS. J. Anal. At. Spectrom. 21 (3) https://doi.org/10.1039/b515908c.

Reynolds, B.C., Aggarwal, J., André, L., Baxter, D., Beucher, C., Brzezinski, M.A., Cardinal, D., 2007. An inter-laboratory comparison of Si isotope reference materials. J. Anal. At. Spectrom. 22 (5), 561–568. https://doi.org/10.1039/b616755a.

Richter, F.M., Mendybaev, R.A., Christensen, J.N., Hutcheon, I.D., Williams, R.W., Sturchio, N.C., Beloso, A.D., 2006. Kinetic isotopic fractionation during diffusion of ionic species in water. Geochim. Cosmochim. Acta 70 (2), 277–289. https://doi.org/10.1016/j.gca.2005.09.016.

Rickert, D., Schlüter, M., Wallmann, K., 2002. Dissolution kinetics of biogenic silica from the water column to the sediments. Geochim. Cosmochim. Acta 66 (3), 439–455. https://doi.org/10.1016/S0016-7037(01)00757-8.

Rutgers Van Der Loeff, M.M., 1980. Nutrients in the interstitial waters of the southern bight of the North Sea. Neth. J. Sea Res. 14 (2), 144–171. https://doi.org/10.1016/0077-7579(80)90019-8.

Santiago Ramos, D.P., Morgan, L.E., Lloyd, N.S., Higgins, J.A., 2018. Reverse weathering in marine sediments and the geochemical cycle of potassium in seawater: Insights from the K isotopic composition (41K/39K) of deep-sea pore-fluids. Geochim. Cosmochim. Acta 236, 99–120. https://doi.org/10.1016/j.gca.2018.02.035.

Schlesinger, W.H., Klein, E.M., Wang, Z., Vengosh, A., 2021. Global biogeochemical cycle of lithium. Glob. Biogeochem. Cycles 35 (8). https://doi.org/10.1029/2021gb006999.

Schulz, H., Zabel, M., 2006. Marine geochemistry: 2 nd revised, updated and extended edition. In: In: Germany: Springer-Verlag. Berlin, Heidelberg, p. 574.

Schulz, K., ThomasArrigo, L.K., Kaegi, R., Kretzschmar, R., 2022. Stabilization of ferrihydrite and lepidocrocite by silicate during Fe(II)-catalyzed mineral transformation: Impact on particle morphology and silicate distribution. Environ. Sci. Technol. 56 (9), 5929–5938. https://doi.org/10.1021/acs.est.1c08789.

Sen, A., Silberberger, M.J., Faust, J.C., Cochrane, S., Renaud, P.E., Reiss, H., 2022. Environmental monitoring data reveals geographic and depth-based differentiation

of benthic fjord communities. Estuar. Coast. Shelf Sci. 268 https://doi.org/10.1016/j.ecss.2022.107803.

Shoenfelt, E.M., Winckler, G., Annett, A.L., Hendry, K.R., Bostick, B.C., 2019. Physical weathering intensity controls bioavailable primary Iron(II) silicate content in major global dust sources. Geophys. Res. Lett. 46 (19), 10854–10864. https://doi.org/10.1029/2019GL084180.

Stuart-Lee, A.E., Mortensen, J., Kaaden, A. S.v.d, Meire, L., 2021. Seasonal hydrography of Ameralik: a southwest greenland fjord impacted by a land-terminating glacier. J. Geophys. Res. Oceans 126 (12). https://doi.org/10.1029/2021jc017552.

Sutton, J.N., André, L., Cardinal, D., Conley, D.J., de Souza, G.F., Dean, J., Swann, G.E. A., 2018a. A review of the stable isotope bio-geochemistry of the global silicon cycle and its associated trace elements. Front. Earth Sci. 5 https://doi.org/10.3389/feart.2017.00112.

Sutton, J.N., de Souza, G.F., García-Ibáñez, M.I., De La Rocha, C.L., 2018b. The silicon stable isotope distribution along the GEOVIDE section (GEOTRACES GA-01) of the North Atlantic Ocean. Biogeosciences 15 (18), 5663–5676. https://doi.org/10.5194/bg-15-5663-2018.

Svahnberg, H., 2010. Deformation Behaviour and Chemical Signatures of Anorthosites: : Examples from Southern West Greenland and South-Central Sweden. (Doctoral thesis, comprehensive summary). Department of Geological Sciences, Stockholm University, Stockholm, p. 340. Retrieved from. http://urn.kb.se/resolve?urn=urn:nbn:se:su:diva-42854DiVA database.

Szilas, K., Hoffmann, J.E., Schulz, T., Hansmeier, C., Polat, A., Viehmann, S., Münker, C., 2016. Combined bulk-rock Hf- and Nd-isotope compositions of Mesoarchaean metavolcanic rocks from the Ivisaartoq Supracrustal Belt, SW Greenland: Deviations from the mantle array caused by crustal recycling. Geochemistry 76 (4), 543–554. https://doi.org/10.1016/j.chemer.2016.09.004.

Tatzel, M., von Blanckenburg, F., Oelze, M., Schuessler, J.A., Bohrmann, G., 2015. The silicon isotope record of early silica diagenesis. Earth Planet. Sci. Lett. 428, 293–303. https://doi.org/10.1016/j.epsl.2015.07.018.

Tréguer, P., Nelson, D.M., Van Bennekom, A.J., DeMaster, D.J., Leynaert, A., Quéguiner, B., 1995. The silica balance in the world ocean: a reestimate. Science 268 (5209), 375–379. https://doi.org/10.1126/science.268.5209.375.

Tréguer, P.J., De La Rocha, C.L., 2013. The world ocean silica cycle. Annu. Rev. Mar. Sci. 5, 477–501. https://doi.org/10.1146/annurev-marine-121211-172346.

Tréguer, P.J., Sutton, J.N., Brzezinski, M., Charette, M.A., Devries, T., Dutkiewicz, S., Rouxel, O., 2021. Reviews and syntheses: the biogeochemical cycle of silicon in the modern ocean. Biogeosciences 18 (4), 1269–1289. https://doi.org/10.5194/bg-18-1269-2021.

Van Cappellen, P., Qiu, L., 1997. Biogenic silica dissolution in sediments of the Southern Ocean. I. Solubility. Deep Sea Res. Part II: Topical Stud. Oceanogr. 44 (5), 1109–1128. https://doi.org/10.1016/S0967-0645(96)00113-0.

Van Cappellen, P., Dixit, S., van Beusekom, J., 2002. Biogenic silica dissolution in the oceans: Reconciling experimental and field-based dissolution rates. Glob. Biogeochem. Cycles 16 (4), 23-21-23-10. https://doi.org/10.1029/2001gb001431.

van Genuchten, C.M., Rosing, M.T., Hopwood, M.J., Liu, T., Krause, J., Meire, L., 2021. Decoupling of particles and dissolved iron downstream of Greenlandic glacier outflows. Earth Planet. Sci. Lett. 576 https://doi.org/10.1016/j.epsl.2021.117234.

Wang, C., Zhu, H., Wang, P., Hou, J., Ao, Y., Fan, X., 2015. Early diagenetic alterations of biogenic and reactive silica in the surface sediment of the Yangtze Estuary. Cont. Shelf Res. 99, 1–11. https://doi.org/10.1016/j.csr.2015.03.003.

Wang, T., Ng, H.C., Hatton, J.E., Hammond, S.J., Woodward, E.M.S., Meire, L., Hendry, K.R., 2023. Hydrographic and Pore Water, Core Incubation, and Sediment Leachate Geochemical Data from Ameralik Fjord and Nuup Kangerlua (Godhäbsfjord) in Southwest Greenland, 2019. PANGAEA.

Ward, J.P.J., Hendry, K.R., Arndt, S., Faust, J.C., Freitas, F.S., Henley, S.F., Tessin, A.C., 2022a. Stable silicon isotopes uncover a mineralogical control on the benthic silicon cycle in the Arctic Barents Sea. Geochim. Cosmochim. Acta 329, 206–230. https://doi.org/10.1016/j.gca.2022.05.005.

Ward, J.P.J., Hendry, K.R., Arndt, S., Faust, J.C., Freitas, F.S., Henley, S.F., Airs, R.L., 2022b. Benthic silicon cycling in the Arctic Barents Sea: a reaction–transport model study. Biogeosciences 19 (14), 3445–3467. https://doi.org/10.5194/bg-19-3445-2022.

Wetzel, F., de Souza, G.F., Reynolds, B.C., 2014. What controls silicon isotope fractionation during dissolution of diatom opal? Geochim. Cosmochim. Acta 131, 128–137. https://doi.org/10.1016/j.gca.2014.01.028.

Windley, B.F., Garde, A.A., 2009. Arc-generated blocks with crustal sections in the North Atlantic craton of West Greenland: Crustal growth in the Archean with modern analogues. Earth-Sci. Rev. 93 (1–2), 1–30. https://doi.org/10.1016/j.earscirev.2008.12.001.

Woodward, E.M.S., Rees, A.P., 2001. Nutrient distributions in an anticyclonic eddy in the Northeast Atlantic Ocean, with reference to nanomolar ammonium concentrations. Deep-Sea Res. II Top. Stud. Oceanogr. 48 (4–5), 775–793. https://doi.org/10.1016/s0967-0645(00)00097-7.

Zheng, X.-Y., Beard, B.L., Reddy, T.R., Roden, E.E., Johnson, C.M., 2016. Abiologic silicon isotope fractionation between aqueous Si and Fe(III)–Si gel in simulated Archean seawater: Implications for Si isotope records in Precambrian sedimentary rocks. Geochim. Cosmochim. Acta 187, 102–122. https://doi.org/10.1016/j.gca.2016.05.012.

Ziegler, K., Chadwick, O.A., Brzezinski, M.A., Kelly, E.F., 2005a. Natural variations of δ30Si ratios during progressive basalt weathering, Hawaiian Islands. Geochim. Cosmochim. Acta 69 (19), 4597–4610. https://doi.org/10.1016/j.gca.2005.05.008.

Ziegler, K., Chadwick, O.A., White, A.F., Brzezinski, M.A., 2005b. δ30Si systematics in a granitic saprolite, Puerto Rico. Geology 33 (10). https://doi.org/10.1130/g21707.1.